ADVANCED ENERGY MATERIALS
www.advenergymat.de

Selective Electrochemical Reduction of CO_2 to Metal Oxalates in Nonaqueous Solutions Using Trace Metal Pb on Carbon Supports Enhanced by a Tailored Microenvironment

Rowan S. Brower, Brian Wuille Bille, Shawn Chiu, Joseph T. Perryman, Libo Yao, Faridat O. Agboola, Cocoro A. Nagasaka, Yinuo Xie, Richard Gomez-Caballero, Ankita Kumari, Elizabeth K. Neumann, Anastassia N. Alexandrova, Charles C. L. McCrory,* and Jesus M. Velázquez**

In this work, the electroreduction of carbon dioxide (CO_2) to oxalate is enabled by incorporating trace metallic lead (Pb) on carbon-based supports (CBS) with polymer overlayers. These composite materials serve as an efficient electrocatalytic system for the facile conversion and storage of CO_2, a pernicious atmospheric pollutant. Results from controlled potential electrolysis experiments indicate that 1) trace metallic Pb on the ppb scale is active toward the reductive coupling of CO_2 to oxalate at comparable Faradaic efficiencies to bulk metallic Pb and 2) polymer encapsulation of this trace metallic Pb leads to promotion of CO_2 reduction (CO_2R) selectively to metal oxalates over other products such as CO. Importantly, metal oxalates are important alternative cementitious materials and precursors for other materials' synthesis applications. The solid products undergo rigorous spectroscopic characterization, including $^{13}CO_2$ labeling experiments, to ensure the metal oxalates are in fact produced from CO_2R. These findings serve as a model for leveraging microenvironment effects to enhance activity and selectivity for CO_2R using trace-metal catalysts for carbon utilization and storage technologies.

1. Introduction

With growing global concerns over rising carbon dioxide (CO_2) emissions, there is an increasing interest in technologies that can capture and redirect industrial CO_2 waste streams toward value-added products, particularly in real-world settings. Carbon capture utilization and storage technologies have emerged as crucial tools for mitigating CO_2 emissions and remediate existing atmospheric CO_2.[1–4] Specifically, point source CO_2 capture and electrochemical conversion to benign, solid products is a promising strategy for CO_2 capture and long-term storage.[5–8] Among the various approaches, the electrochemical reduction of CO_2 to oxalate ($C_2O_4^{2-}$) has gained attention due to its ability to convert CO_2 into stable, solid products that can be easily stored and utilized.[9–12]

R. S. Brower, B. Wuille Bille, J. T. Perryman, C. A. Nagasaka, Y. Xie, A. Kumari, E. K. Neumann, J. M. Velázquez
Department of Chemistry
University of California-Davis
Davis, CA 95616, USA
E-mail: jevelazquez@ucdavis.edu

S. Chiu, A. N. Alexandrova
Department of Chemistry and Biochemistry
University of California-Los Angeles
Los Angeles, CA 90095-1569, USA
E-mail: alexandrova@g.ucla.edu

L. Yao
Department of Chemical Engineering
University of Michigan
Ann Arbor, MI 48109, USA

F. O. Agboola, C. C. L. McCrory
Department of Chemistry
University of Michigan
Ann Arbor, MI 48109-1055, USA
E-mail: cmccrory@umich.edu

R. Gomez-Caballero
Department of Chemistry
Universidad de Puerto Rico Recinto de Río Piedras
San Juan PR 00931-3346, Puerto Rico

C. C. L. McCrory
Macromolecular Science & Engineering Program
University of Michigan
Ann Arbor, MI 48109-2102, USA

The ORCID identification number(s) for the author(s) of this article can be found under https://doi.org/10.1002/aenm.202501286

© 2025 The Author(s). Advanced Energy Materials published by Wiley-VCH GmbH. This is an open access article under the terms of the Creative Commons Attribution-NonCommercial License, which permits use, distribution and reproduction in any medium, provided the original work is properly cited and is not used for commercial purposes.

DOI: 10.1002/aenm.202501286

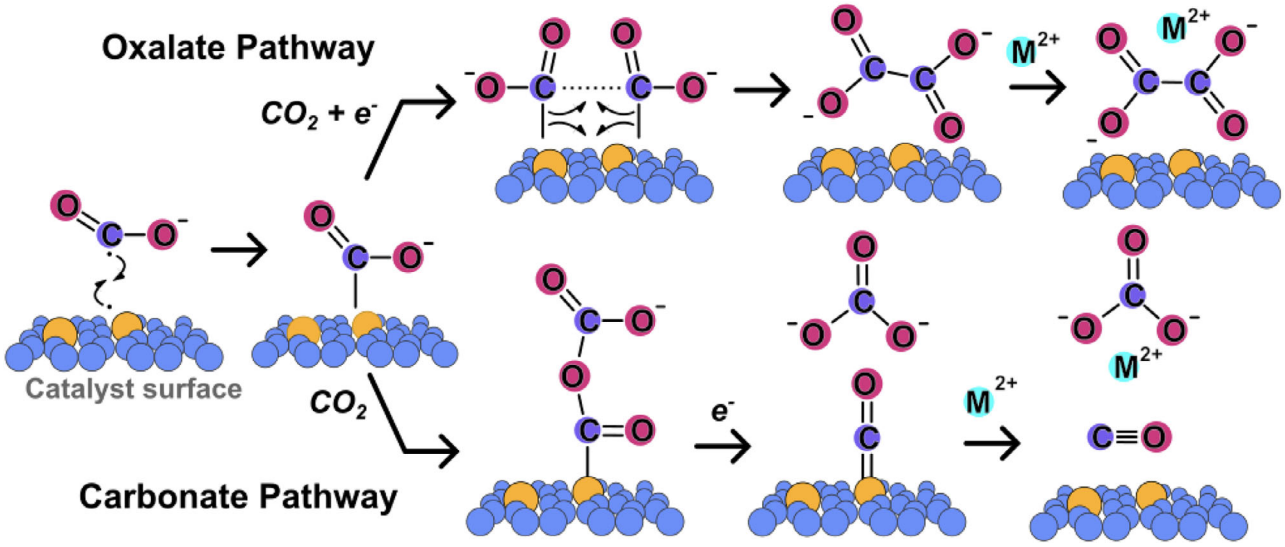

Scheme 1. Proposed mechanisms for the reduction of CO_2 to oxalate and carbonate in nonaqueous aprotic solvents.

In such a reaction, CO_2 is first converted into CO_2 radical anions at an electrode surface ($*CO_2^{\bullet-}$), and these $*CO_2^{\bullet-}$ couple to form $C_2O_4^{2-}$ as shown **Scheme 1**. We note that the specific location of C—C coupling in the oxalate pathway shown in Scheme 1 is still a matter of scientific discussion in aprotic solvents, i.e., whether the C—C coupling occur between two $*CO_2^{\bullet-}$ adsorbed onto the electrode surface within the double layer,[10,13,14] or by two desorbed $CO_2^{\bullet-}$ in the reaction–diffusion layer.[15–17] The $C_2O_4^{2-}$ product can then be precipitated with an M^{2+} cation to produce a solid MC_2O_4, which holds promise for a variety of applications, including as precursors in material synthesis, soil additives, and alternative cementious materials.[18–21]

In this scheme, CO_2 to $CO_2^{\bullet-}$ is the primary elementary step crucial for the formation of all C^{2+} products of electrochemical CO_2 reduction (CO_2R).[22,23] However, for the oxalate pathway to proceed, the electrode surface and surrounding microenvironment must promote the "coupling" of the adsorbed $*CO_2^{\bullet-}$ preferentially to its further reduction to a surface carbonyl. Furthermore, this general reductive–coupling pathway can lead to the reduction of other valuable derivatives such as glyoxylic acid ($C_2H_2O_3$), glycolic acid ($C_2H_4O_3$), glyoxal ($C_2H_2O_2$), glycolaldehyde ($C_2H_4O_2$), and ethylene glycol ($C_2H_6O_2$)—all of which are valuable commodity chemicals in the production of agrochemicals, cosmetics, and polymers.[21,24]

Traditionally, the synthesis of oxalate via $CO_2^{\bullet-}$ coupling has been demonstrated using bulk metallic electrodes, primarily Pb in nonaqueous electrolytes.[14,25–27] In the case of CO_2R on Pb electrodes, researchers have improved the catalytic activity and selectivity for $C_2O_4^{2-}$ production by changing the solvent, supporting electrolyte, and roughness of the electrode surface.[24] However, although Pb is abundant and relatively low cost compared to most other transition metals,[28] it is also an environmental contaminant that impacts both environmental and human health.[29,30] Therefore, a major goal for oxalate-forming systems is to design new catalyst systems that have similar activity to existing bulk Pb-based systems, but with significantly decreased Pb loading. Designing new catalyst systems with decreased Pb loading will both increase mass activity (MA) and reduce potential environmental contamination.

To enable similar CO_2R activities by catalyst systems with decreased Pb loadings, we will modulate the chemical microenvironment. Tuning the chemical microenvironment surrounding catalyst active sites to control local substrate concentration and stabilize and confine reactive intermediates has shown promise in enhancing catalytic activity for the CO_2R, especially to C_2^+ products.[31–42] A crucial strategy to modulate local microenvironment is coating catalysts with polymer/ionomer overlayers to control proton delivery and tune local electrostatic fields near the catalyst active sites.[31,43–48] We will adapt this strategy to enhance the activity of low loadings of Pb catalysts for the selective conversion of CO_2 to $C_2O_4^{2-}$. Although microenvironment control has been used previously to enhance CO_2R activity, to the best of our knowledge, this work is the first example of tuning microenvironment to specifically enhance oxalate production.

In this study, we report that coating Pb catalysts with an overlayer of the hydrophobic fluoropolymer polytetrafluoroethylene (PTFE) enables the selective reduction of CO_2 to $C_2O_4^{2-}$ with high activity (≈130 A g_{Pb}^{-1}) and selectivity (≈80% $C_2O_4^{2-}$) at ultralow loadings of Pb (≤160 ng cm^{-2}) found in commercial carbon sources. It has been previously reported that trace metal impurities can contribute significantly to catalytic current densities often more so than the proposed catalyst,[39,49–52] even at concentrations as low as parts per billion (ppb).[53] In our work, we are repurposing trace Pb impurities in commercial carbon supports for the CO_2R by controlling their chemical microenvironment to promote C—C coupling for C_2-product generation. Importantly, we show that the polymer-coated trace-Pb catalyst systems operate with comparable activity and selectivity to bulk Pb electrocatalysts.

Using our trace-Pb catalyst system, we demonstrate the electrochemical synthesis of various metal oxalates including ZnC_2O_4, CoC_2O_4, FeC_2O_4, and MnC_2O_4. The formation of Co, Fe, and Mn oxalates, in particular, holds promise for their use in alternative cement production, offering a dual benefit of CO_2

© 2025 The Author(s). Advanced Energy Materials published by Wiley-VCH GmbH

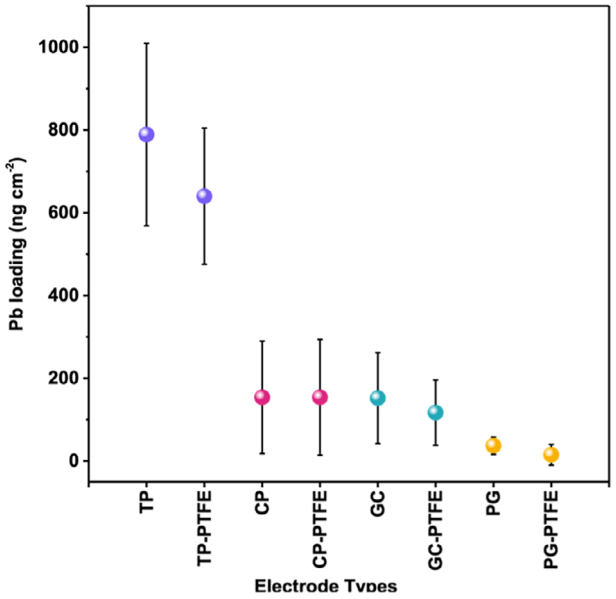

Figure 1. Pb loading of four different commercial carbon electrodes with and without a spray-deposited PTFE coating. The Pb loadings were measured by etching the electrodes in trace-metal grade 5% HNO_3 and determining the Pb concentration in the etchant solution. Each data point is an average from measurements on prepared electrodes, and the reported error bars are standard deviations. Each prepared electrode was ≈1 cm^2. All data from this figure are also included in Table S1 (Supporting Information).

mitigation and sustainable construction and highlighting the versatility of the trace-Pb catalyst system for carbon utilization. This work provides a proof-of-concept demonstration of how microenvironment engineering can enhance the performance of trace-metal catalysts for CO_2 reduction, while broadening the applicability of these technologies under more challenging operational conditions. Our findings serve as a model for leveraging microenvironment effects to enhance CO_2R activity and selectivity, demonstrating the potential of trace-metal catalysts in the development of efficient and sustainable CO_2 utilization and storage technologies.

2. Results and Discussion

2.1. Electrocatalytic CO_2R at Commercial Carbon Electrodes with Different Trace-Pb Loadings Using a Zn Counter Electrode

Four commercial carbon electrodes were investigated for CO_2R: toray paper (TP), carbon paper (CP), glassy carbon (GC), and highly oriented pyrolytic graphite (PG). The Pb loading on each as-purchased carbon support was characterized by first etching the carbon support with 5 wt% trace-metal grade nitric acid (HNO_3) in ultrapure water and investigating the etching solution by inductively coupled plasma-mass spectrometry (ICP-MS). The loading of each support is shown in **Figure 1** and summarized in Table S1 (Supporting Information). Each type of carbon electrode was also spray-coated with PTFE, and the Pb loading in the PTFE-coated electrodes was also investigated by ICP-MS (TP-PTFE, CP-PTFE, GC-PTFE, and PG-PTFE) and reported in Figure 1 and Table S2 (Supporting Information). As expected, adding a PTFE coating had no discernible effect on the trace Pb loading amount; the measured Pb loading for each carbon support and its PTFE-coated analog were approximately equal. The trace amounts of Pb found in these carbon electrodes are contaminants from their production.[54] However, leveraging trace Pb active sites in commercially available carbon electrodes for $C_2O_4^{2-}$ production offers a promising pathway for scalable oxalate synthesis, with potential for future integration into deployable technologies such as electrochemical CO_2 capture and conversion units for sustainable manufacturing of alternative cementitious materials.

Initial electrocatalytic performance for CO_2R of each electrode was first measured using linear sweep voltammetry (LSV) in a single-compartment electrochemical cell with the specific carbon electrode or PTFE-coated electrode as the working electrode, a Zn counter electrode, and an Ag/AgCl reference electrode (0.04 M LiCl and 0.1 M tetrabutylammonium perchlorate ($n$$Bu_4ClO_4$) in acetonitrile (MeCN)) (Figure S1, Supporting Information). The electrolyte was 0.1 M $n$$Bu_4ClO_4$ in anhydrous MeCN with no added proton source, and steps were taken to exclude water from the experimental setup. Only trace amounts of water (<0.066 mM) were detected in the electrolyte solution via Karl Fischer titration. The Ag/AgCl reference electrode was externally referenced to the ferrocene/ferrocenium couple (Fc/Fc^+) as described in Figure S2 (Supporting Information), and all potentials in this work are reported against Fc/Fc^+ following the International Union of Pure and Applied Chemistry (IUPAC) recommendations for reporting potentials in nonaqueous electrolytes.[55,56] A Zn counter electrode was tested first because prior literature demonstrated effectiveness in precipitating the oxalate anion. LSVs were conducted both under Ar and under CO_2 (**Figure 2**a,b). For the carbon electrodes with no PTFE coating, the magnitude of the current is larger under static CO_2 compared to the current under static Ar, suggesting catalytic CO_2R occurs under a CO_2 atmosphere. With PTFE, there was a general suppression of CO_2R catalytic activity for each carbon electrode compared to the activity of the analogous bare electrode.

Controlled potential electrolysis (CPEs) were then completed at −1.9 V versus Fc/Fc^+ for all electrodes in a sealed single-compartment electrochemical cell and 0.1 M $n$$BuClO_4$ electrolyte in MeCN. A potential of −1.9 V versus Fc/Fc^+ was chosen for the CPEs because previous studies of CO_2R of bulk Pb electrodes with a Zn counter electrode show the highest Faradaic efficiency (FE) for $C_2O_4^{2-}$ production at this potential.[13,14,25,26] The Zn counter electrode serves as a sacrificial anode (SA) that forms Zn^{2+} in solution, precipitating any electrochemically generated $C_2O_4^{2-}$ as insoluble ZnC_2O_4. We observed the formation of solid precipitates during the CPEs for all eight electrodes investigated, and the solid precipitates were characterized by attenuated total reflection-Fourier transform infrared spectroscopy (ATR-FTIR) (Figure 2c,d). For TP, TP-PTFE, and CP-PTFE, the solid precipitate is assigned as ZnC_2O_4 based on the ATR-FTIR spectra. A proposed mechanism for $C_2O_4^{2-}$ formation from CO_2R in anhydrous media is shown in Scheme 1. For the other electrodes investigated (CP, GC, GC-PTFE, PG, and PG-PTFE), the solid product more closely resembled $(ZnCO_3)_2$•$(Zn(OH)_2)_3$ (Figure S3, Supporting Information). $(ZnCO_3)_2$•$(Zn(OH)_2)_3$ is the final product from CO production according to Figure S4 and Scheme S1 (Supporting Information).

© 2025 The Author(s). Advanced Energy Materials published by Wiley-VCH GmbH

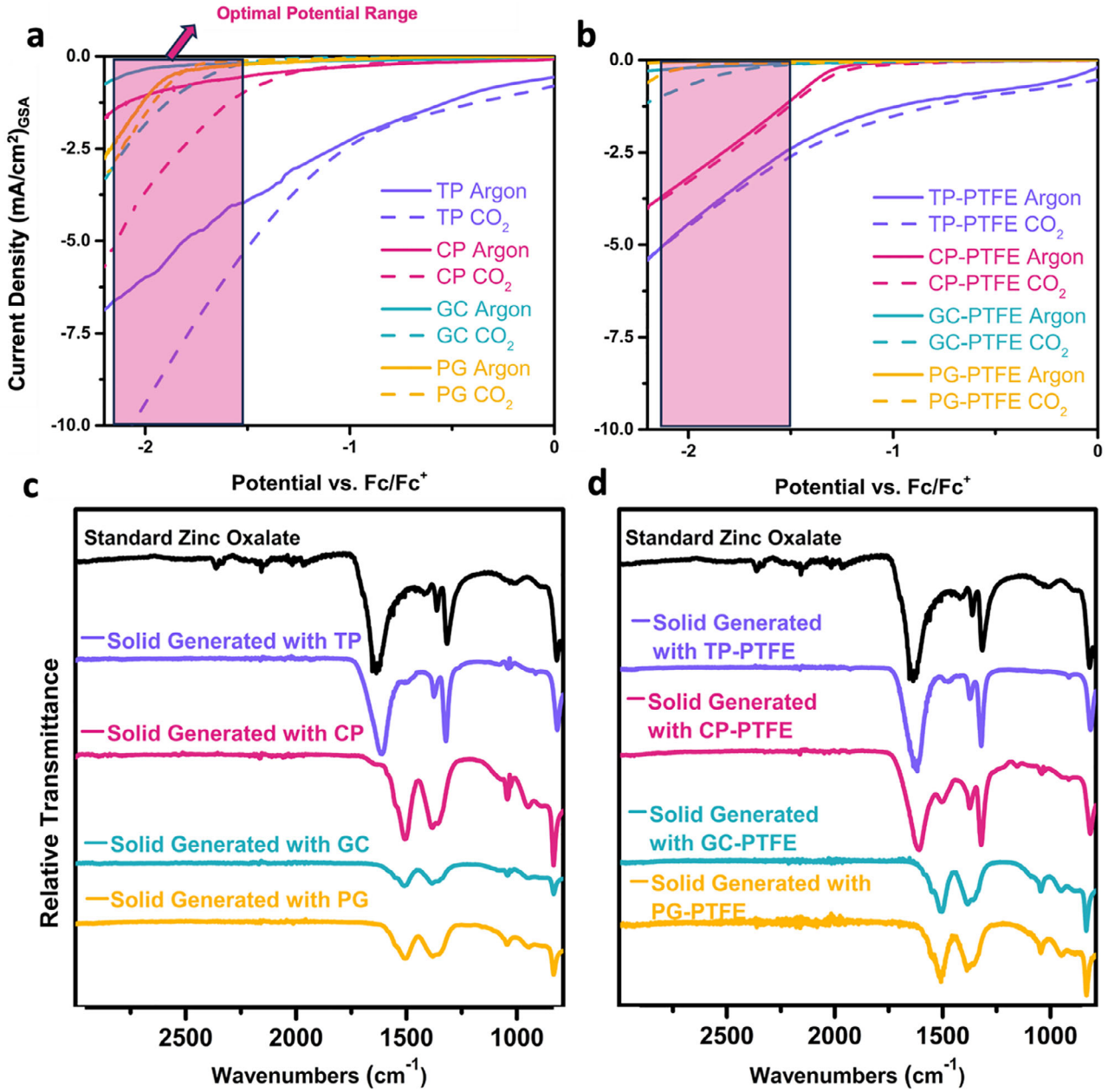

Figure 2. a) LSVs of all carbon-based supports (CBS) purchased as is and b) with additional PTFE layers under Ar and CO_2 streams. Representative ATR-FTIR spectra of solid products from CO_2R electrolysis at −1.9 V versus Fc/Fc^+ at c) carbon electrodes as is and d) the same carbon electrodes with PTFE overlayers. The solid precipitates from the electrolyses at TP, TP-PTFE, and CP-PTFE show characteristic peaks consistent with ZnC_2O_4: C═O asymmetrical stretch (1625 cm^{-1}), C—O symmetrical stretch (1375 cm^{-1}), and O═C—O angular deformation (1325 cm^{-1}). The solid precipitates from electrolysis at CP, GC, GC-PTFE, PG, and PG-PTFE have peaks consistent with $(ZnCO_3)_2 \bullet (Zn(OH)_2)_3$, a product of CO_2R to CO.

The fact that only TP, TP-PTFE, and CP-PTFE produced ZnC_2O_4 during electrolysis suggests that only the electrodes with the highest Pb loadings are active for CO_2R. Interestingly, the CO_2R at CP did not produce ZnC_2O_4, suggesting that the PTFE overlayer modifies the catalyst microenvironment to facilitate CO_2R to $C_2O_4^-$. We propose that the PTFE overlayer inhibits proton transport to the Pb active sites, thereby facilitating C—C coupling between the adsorbed $*CO_2^{\bullet-}$ intermediates to form $C_2O_4^{2-}$ instead of protonation and reduction to produce CO and H_2O. The effect of polymer overlayers to control substrate transport and modulate product distribution has been recently reported for both solid-state and molecular CO_2R catalysts.[32,33,38,43–48] It is worth noting that GC and PG electrodes show no CO_2R to $C_2O_4^{2-}$ activity even with PTFE overlayers. In addition to having a lower Pb loading than TP and CP, GC and PG also have a lower surface area. Thus, we cannot exclude the possibility that surface morphology also has an impact on the $C_2O_4^{2-}$ product selectivity. Certainly, higher substrate porosity has been

© 2025 The Author(s). Advanced Energy Materials published by Wiley-VCH GmbH

reported to drive CO_2R product selectivity toward more highly reduced products and/or C—C coupled products, presumably by modulating the transport of products and retention of intermediates near the catalyst sites in more porous electrodes.[57,58]

We performed contact angle (CA) measurements on all eight electrodes using both 18 MΩ water and 0.1 M nBu$_4$ClO$_4$ in MeCN (Table S2, Supporting Information). In general, the water CA (WCA) on each electrode is larger than that of the nonaqueous electrolyte, indicating that the nonaqueous electrolyte has enhanced electrolyte–electrode interactions compared to water. Notably, adding PTFE to the TP electrode decreases both the water CA and nonaqueous electrolyte CA (ECA). Similarly, adding PTFE to CP also leads to a smaller water CA, although the nonaqueous electrolyte CA is not measurable due to rapid solution uptake by both CP and CP-PTFE. However, in the case of GC and PG electrodes, adding PTFE results in a large increase in the water CA, but a more modest change in the nonaqueous electrolyte CA. These contact angle results suggest that adding PTFE to the TP and CP electrodes improves wettability and solution–electrode interactions of the resulting electrode, but adding PTFE to GC and PG reduces wettability of the resulting electrode. Overall, these substrate-specific responses further support that PTFE does alter the surface chemical microenvironment in a way that is dependent on the underlying carbon support.

We further investigated and quantified the product distribution for the three oxalate-forming electrodes TP, TP-PTFE, and CP-PTFE, and the nonpolymer coated analog CP. CPEs were conducted in a sealed cell as described above, and 100 C was passed in each electrolysis with each experiment taking between 5 and 8 h (Figure S4, Supporting Information). For each CPE, solid, gaseous, and solution-phase products were investigated. Gaseous CO and H_2 products were detected and quantified using gas chromatography- thermo conductivity detector (GC-TCD)(Figure S5, Supporting Information). Solution-phase product analysis was completed with ^{1}H nuclear magnetic resonance (NMR) and ^{13}C NMR spectroscopy, but no solution-phase products were detected from CPEs at any of the four electrodes as shown in Figure S6 (Supporting Information). For TP, TP-PTFE, and CP-PTFE, solid products were washed with 0.1 M NaOH to remove any trace $(ZnCO_3)_2$• $(Zn(OH)_2)_3$; the composition of the product as ZnC_2O_4 was confirmed with ATR-FTIR; and the mass of the product was measured with gravimetric analysis. For CP electrodes, the solid product was confirmed as $(ZnCO_3)_2$•$(Zn(OH)_2)_3$ via NMR, and the mass of the $ZnCO_3$ was then calculated according to Equation (1)

$$m_{ZnCO_3} = m_{(ZnCO_3)\cdot(Zn(OH)_2)_3} \times 0.228 \quad (1)$$

where $m_{ZnCO_3\cdot(Zn(OH)_2)_3}$ is the measured mass of $(ZnCO_3)_2$•$(Zn(OH)_2)_3$, m_{ZnCO_3} is the calculated mass of $ZnCO_3$, and 0.228 is the mass fraction of $ZnCO_3$ in $(ZnCO_3)_2$•$(Zn(OH)_2)_3$. The FE of each product was calculated according to Equation (2)

$$FE = \frac{n \cdot F \cdot mol_{product}}{Q} \times 100\% \quad (2)$$

where n is the number of electrons, F is Faraday's constant, $mol_{product}$ is the number of moles of products measured experimentally, and Q = 100 C is the charge passed during the CPE. The average partial current density (PCD) going to a specific product during the CPE and normalized to geometric surface area was estimated according to Equation (3)

$$j_{avg} = \frac{Q \cdot FE}{t \cdot A} \quad (3)$$

Here Q = 100 C is the charge passed, FE is the Faradaic Efficiency to the specific product, t is the time of the electrolysis, and A is the geometric surface area of the working electrode.

To determine the optimal applied potential for the CPE experiments, we measured the product distribution and PCD values for each product from the CPE experiment for TP and TP-PTFE (**Figure 3**), which we expect to be the more active and selective catalysts according to the preliminary electrolysis results in Figure 2. Of the three potentials investigated between −1.8 and −2.1 V versus Fc/Fc$^+$ (data summarized in Table S3 in the Supporting Information), the maximum FE for ZnC_2O_4 is observed at −1.9 V versus Fc/Fc$^+$. We do observe larger magnitude PCD for ZnC_2O_4 production at −2.1 V versus Fc/Fc$^+$ compared to −1.9 V versus Fc/Fc$^+$, but the FE for ZnC_2O_4 is smaller at the more negative potential. This decrease in efficiency at higher overpotentials suggests that a portion of the charge is being consumed by competing side reactions, such as electrolyte degradation, which has been noted in the literature for similar systems.[59] We chose to select for selectivity over activity for subsequent comparative studies, and so we chose −1.9 V versus Fc/Fc$^+$ as the potential for our subsequent CPE measurements comparing product distributions (**Figure 4**).

The product distributions and PCD for each product from the CPE experiments at −1.9 V versus Fc/Fc$^+$ for TP, TP-PTFE, CP, and CP-PTFE are shown in **Figure 4** and summarized in Table S4 (Supporting Information). Note that TP and TP-PTFE both show high selectivity for ZnC_2O_4 production, with TP-PTFE showing slightly higher FE for ZnC_2O_4 for and significantly lower FE for CO, but at slightly lower PCD. This result suggests that the PTFE overlayer enhances selectivity for C—C coupling for $C_2O_4^{2-}$, but with a corresponding slight decrease in catalyst activity. This slight decrease in activity could be due to inhibited access of reactant or electrolyte to the Pb active sites due to the polymer overlayers.[38,43,60] However, the effect of PTFE on the CO_2R performance of CP is much more pronounced. CP shows no activity for ZnC_2O_4, instead producing only CO and its corresponding solution species $ZnCO_3$. However, the polymer-coated CP-PTFE electrode produces ZnC_2O_4 with ≈73% FE and a PCD similar to that of TP-PTFE. This drastic change in selectivity illustrates the crucial role of the polymer overlayer in facilitating C—C bond formation for ZnC_2O_4 production. For comparison, we also measured the CO_2R activity and selectivity of a bulk Pb electrode, also shown in Figure 4. The PCD and FE for ZnC_2O_4 for TP, TP-PTFE, and CP-PTFE are comparable to that of the bulk Pb electrode, suggesting that we can achieve the same overall activity for CO_2R to ZnC_2O_4 using trace amounts of Pb on carbon supports, especially when we use a fluoropolymer to control the microenvironment around the catalyst. The small amounts of H_2 (<3% FE) detected in each sample are attributed to the reduction of trace water (<0.066 mM) in our electrolyte solutions.

© 2025 The Author(s). Advanced Energy Materials published by Wiley-VCH GmbH

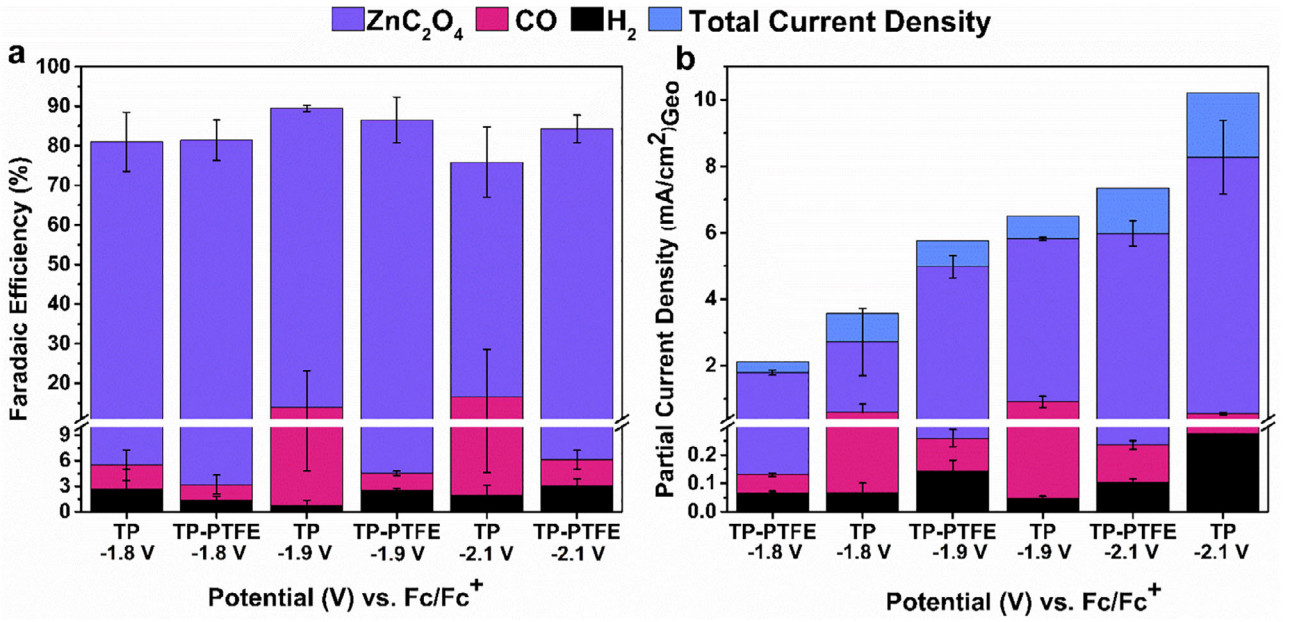

Figure 3. Product distributions from CPE measurements for the CO_2R by TP and TP-PTFE in CO_2-saturated 0.1 M nBuClO$_4$ in MeCN. CPEs were conducted for 100 C at three different potentials: −1.8, −1.9, and −2.1 V versus Fc/Fc$^+$. a) Faradaic efficiencies and b) absolute value of average PCD for the CO_2R products. All data in this figure are also included in Table S3 (Supporting Information).

The product selectivity for $C_2O_4^{2-}$ over CO_3^{-} can be sensitive to several parameters,[61,62] including cations or water molecules near the electrode surface that can stabilize adsorbed $*CO_2^{\bullet-}$, promoting CO_3^{-} formation over C—C coupling.[62] We postulate that the hydrophobic PTFE overlayer may be producing a favorable microenvironment for CO_2R to $C_2O_4^{2-}$ by both 1) helping to retain $CO_2^{\bullet-}$ at or near the electrode surface to promote C—C coupling, and 2) inhibiting the transport of electrolyte cations such as nBu$_4^+$ and trace water to the electrode that could stabilized adsorbed $*CO_2^{\bullet-}$ and facilitate $C_2O_4^{2-}$ production.

To assess the influence of PTFE loading on oxalate production, we systematically varied the amount of PTFE added to carbon paper electrodes and evaluated the resulting electrochemical performance (see Figures S7 and S8 in the Supporting Information). Among the tested loadings—0, 9.4, and 18.8 mg cm^{-2}—9.4 mg cm^{-2} PTFE was identified as the optimal condition, achieving a favorable balance between oxalate selectivity and current density. Increasing the PTFE loading to 18.8 mg cm^{-2} leads to a marginal increase in Faradaic efficiency for oxalate production, but with a noticeable decrease in current density, possibly due to decreased

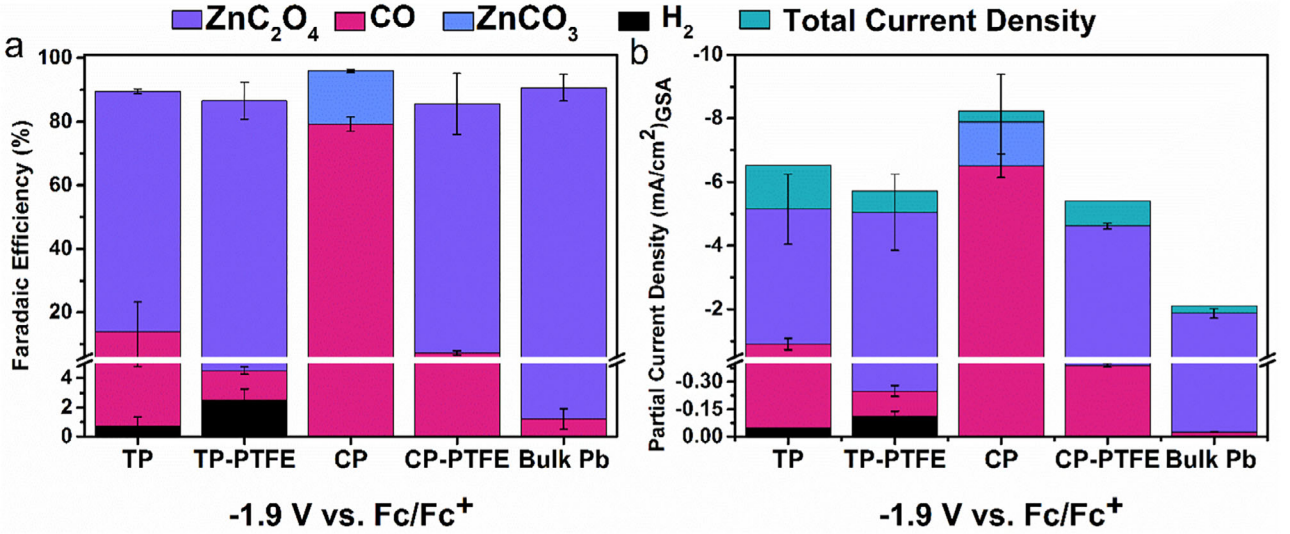

Figure 4. Product distributions from CPE measurements for the CO_2R by TP, TP-PTFE, CP, and CP-PTFE in CO_2-saturated 0.1 M nBuClO$_4$ in MeCN. CPEs were conducted for 100 C. a) Faradaic efficiencies and b) average PCD for the CO_2R products. All data in this figure are also included in Table S4 (Supporting Information).

© 2025 The Author(s). Advanced Energy Materials published by Wiley-VCH GmbH

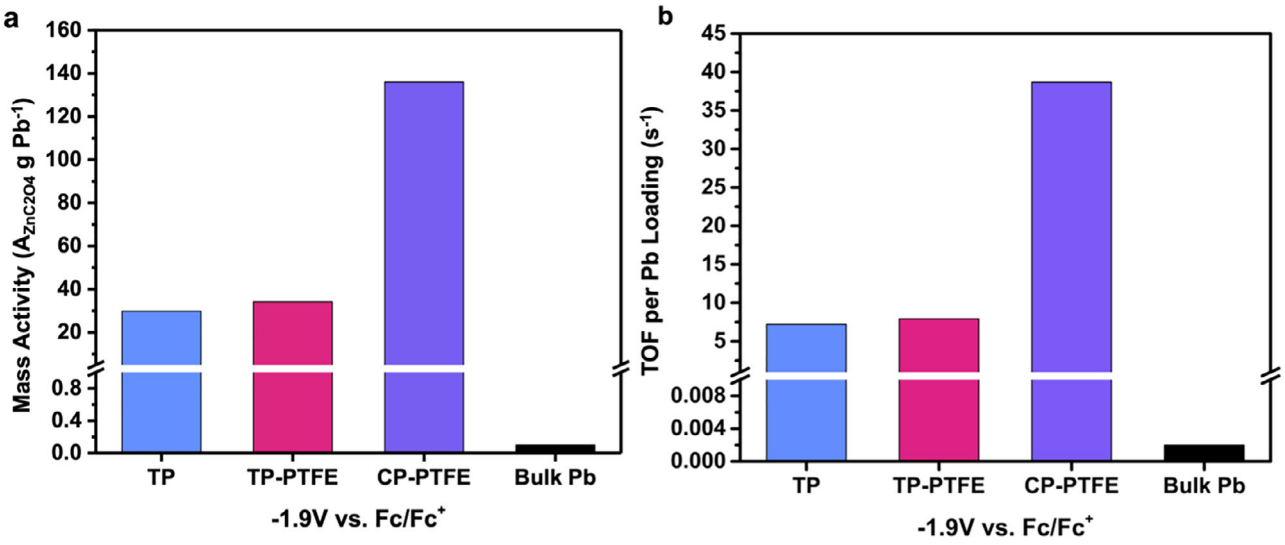

Figure 5. a) Apparent mass activity and b) turn over frequency (TOF) for CO_2R to ZnC_2O_4 normalized for total Pb loading.

accessibility of the catalyst sites to reactants.[38,43,60] These findings highlight the importance of tuning polymer content to modulate the catalyst microenvironment without compromising overall activity.

We can also estimate the apparent turnover frequency (TOF), shown in **Figure 5**, of the different electrodes for moles of ZnC_2O_4 per total Pb loading based (summarized in Table S5 in the Supporting Information) on Equation (4)

$$\mathrm{TOF} = \frac{\mathrm{mol}_{\mathrm{ZnC_2O_4}}}{t \cdot \left(m_{\mathrm{Pb}}/M_{\mathrm{m,Pb}}\right)} \tag{4}$$

where $\mathrm{mol}_{\mathrm{ZnC_2O_4}}$ is the moles of the ZnC_2O_4 produced in the electrolysis, t is the time of the electrolysis, $\dot{m}_{\mathrm{Pb}}$ is the mass of Pb loaded onto the electrode as determined by ICP-MS, and $M_{\mathrm{m,Pb}} = 207.2\ \mathrm{g\ mol^{-1}}$ is the molar mass of Pb. Note that for our bulk Pb electrodes, m_{Pb} was taken as the mass of the electrode. The CP-PTFE electrode had the largest apparent TOF, suggesting that this electrode enables rapid production of ZnC_2O_4 at the lowest Pb loadings. TP and TP-PTFE had similar apparent TOFs, and all carbon-based electrodes with trace Pb had much higher apparent TOFs than bulk Pb. These results suggest that larger loadings of Pb do not necessarily translate to higher overall activity for the CO_2R reaction.

We also estimated MA, as shown in Figure 5, of the different electrodes for moles of ZnC_2O_4 per mass of Pb based on Equation (5)

$$\mathrm{MA} = \frac{A_{\mathrm{ZnC_2O_4}}}{m_{\mathrm{Pb}}} \tag{5}$$

where $A_{\mathrm{ZnC_2O_4}}$ is the PCD of the ZnC_2O_4 produced in the electrolysis and m_{Pb} is the mass of Pb loaded onto the electrode as determined by ICP-MS. As with the TOF calculations, the CP-PTFE had the largest MA followed by TP and TP-PTFE.

2.2. Measuring CO_2R Activity at Different Pb Loadings

To determine the minimum level of trace Pb loading capable of reducing CO_2 to MC_2O_4 (a Zn counter electrode was chosen as representative for all SAs), we conducted a Pb loading dependence study spanning four orders of magnitudes of Pb loadings from 0.01 to 10 mg cm^{-2} Pb on CP with and without at PTFE overlayer, as shown in **Figure 6**. We also measured an electrode with no Pb added (0 mg cm^{-2} Pb) for comparison. We chose 0.01 mg cm^{-2} Pb as our lower limit for this study because it was the lowest mass loading we were able to accurately deposit on CP using our deposition techniques. Prior to preparation, each CP electrode was etched with trace-metal grade HNO_3 to remove all residual Pb, and then the known amount of Pb was added to the CP electrode. Each electrode was investigated by CPEs at −1.9 V versus Fc/Fc^+ in 0.1 M nBu$_4$ClO$_4$ in MeCN under a CO_2 atmosphere. 100 C was passed in each CPE, and the products were quantified and characterized analogously to the other quantitative CPE measurements described above.

All electrodes with added Pb produced ZnC_2O_4, and the PTFE-coated electrodes produced higher Faradaic efficiencies of ZnC_2O_4 than their non-polymer-coated analogs. This was particularly noticeable at the lowest loading of 0.01 mg Pb, where the 0.01 mg CP-PTFE electrode had 30% larger FE for ZnC_2O_4 compared to 0.01 mg CP. Note that CO is the preferred product for the electrodes with no added Pb (e.g., 0-mg-CP and 0 mg-CP-PTFE). The key takeaway from these experiments is that at relatively high Pb loadings of ≥0.1 mg cm^{-2}, the polymer overlayers do not have a strong effect on the product selectivity for ZnC_2O_4. However, at Pb loadings 0.01 mg cm^{-2} ≥ Pb ≥ 0 mg cm^{-2}, the hydrophobic PTFE overlayers have an appreciable effect on increasing the selectivity toward oxalate production. We note that this is range of Pb loadings we find in untreated commercial carbon papers. When no Pb is present (0 mg-CP and 0 mg-CP-PTFE), no ZnC_2O_4 is formed even with the addition of polymer layers.

© 2025 The Author(s). Advanced Energy Materials published by Wiley-VCH GmbH

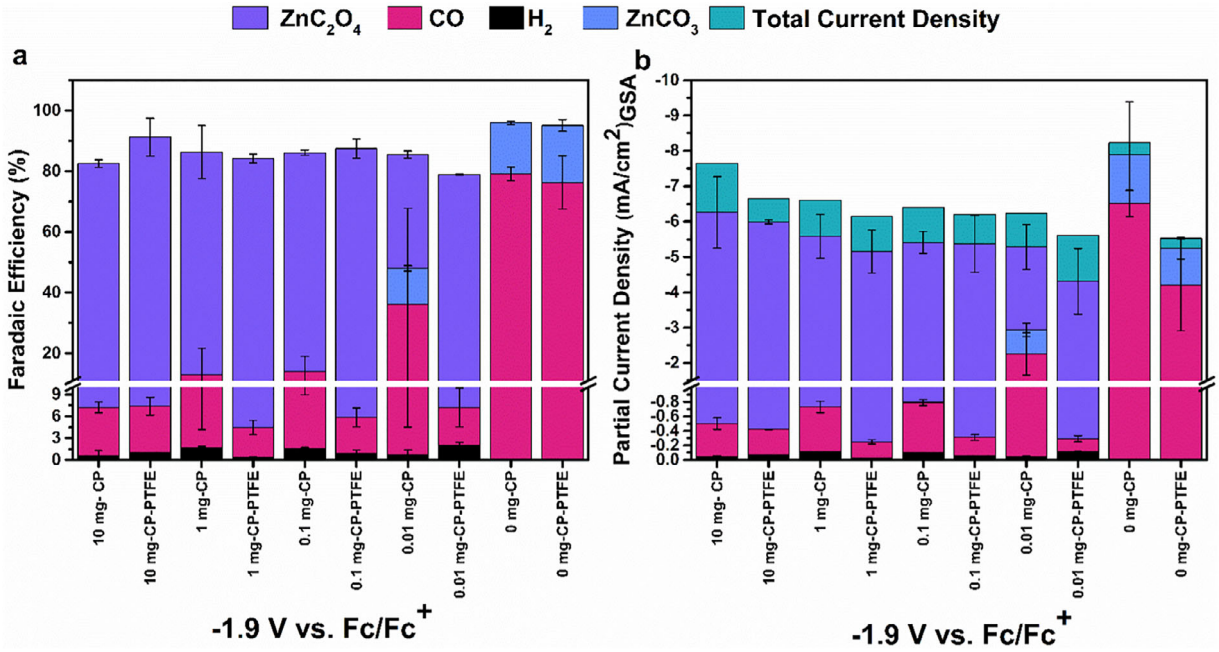

Figure 6. a) Product distribution and b) partial current density for carbon paper electrodes with varying Pb loadings (0, 0.01, 0.1, 1, and 10 mg cm^{-2}), both with and without PTFE polymer overlayers. All data in this figure are also included in Table S6 (Supporting Information).

2.3. Feasibility of CO_2R with Nonaggregated Pb on Carbon Supports

To test the viability of the oxalate pathway proposed in Scheme 1 on carbon electrodes containing trace Pb and to determine whether such a trace-Pb catalyst can drive C—C coupling under hydrophobic conditions, we performed grand canonical density functional theory (GCDFT) calculations in implicit acetonitrile (**Figure 7a**). The electrode was modeled as Pb-doped graphite with two substitutional lead atoms. We note that while this surface cannot yet be confirmed experimentally, it provides a proxy for exploring oxalate generation via C—C coupling on our trace-Pb catalyst system. The system's work function was computed relative to the initial charge of the adsorbate. The top view of the optimized geometries is provided in Figure 7b–e, and the side view is provided in Figure S9a–d (Supporting Information). As shown in Figure 7a, the electronic grand canonical free energy profile is uniformly negative, signaling a thermodynamically feasible mechanism. The first CO_2 activation step is already downhill because the acetonitrile continuum stabilizes the $CO_2\bullet^-$

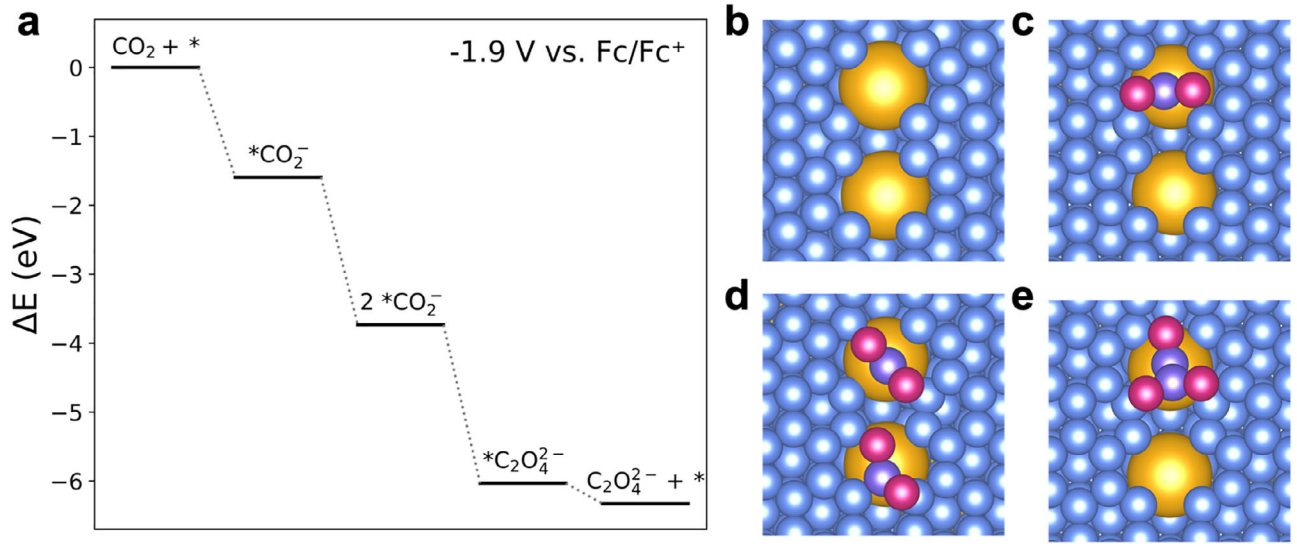

Figure 7. a) Thermodynamic reaction pathway of the proposed oxalate pathway on Pb-doped graphite at −1.9 V versus Fc/Fc^+. Top view of the optimized structures of b) the bare surface, c) $*CO_2^-$, d) $2*CO_2^-$, and e) $*C_2O_4^{2-}$.

© 2025 The Author(s). Advanced Energy Materials published by Wiley-VCH GmbH

radical far more effectively than neutral, nonpolar CO_2.[63,64] The subsequent radical coupling, oxalate formation, and desorption steps are likewise exergonic, further supporting this reaction pathway.

2.4. Electrochemical Synthesis of Co, Fe, and Mn Oxalate Salts

To investigate further the practical applications of the trace-Pb catalyst for oxalate production, we used the TP-PTFE catalyst to synthesize a series of metal oxalates commonly used as alternative cementitious materials in sustainable cement production.[18–20] Specifically, we changed the Zn SA for Co, Fe, and Mn to produce CoC_2O_4, FeC_2O_4, and MnC_2O_4 solid oxalate salts, respectively. TP-PTFE was chosen as the catalyst system of choice due to its high Faradaic efficiency for oxalate production using Zn SAs. Electrocatalytic performance evaluation measurements were conducted for CO_2R using analogous methods as outlined above, with the only difference being the change in the metal SA. LSVs conducted for TP-PTFE with all three SAs under both Ar and CO_2 are shown in Figure S10a (Supporting Information), and all three systems show increased current densities under CO_2 atmospheres compared to their Ar atmospheres. CPEs conducted at −1.9 V versus Fc/Fc^+ in sealed, single-compartment electrochemical cells, as described above, showed formation of insoluble products for all three SAs used. The solids formed during CPE were initially characterized by ATR-FTIR (Figure S10b–d, Supporting Information) and were consistent with the formation of CoC_2O_4, Fe_2O_4, and Mn_2O_4.

We then conducted CPEs at various potentials to determine a potential-dependent production distribution of each metal oxalate salt. These were conducted in a sealed cell as described above, and 100 C was passed in each electrolysis. For each CPE, solid, gaseous, and solution phase products were quantified and characterized analogously to the other quantitative CPE measurements described above. The product distribution and PCD for CO_2R to CoC_2O_4 (**Figure 8**a,b), FeC_2O_4 (Figure 8c,d), and MnC_2O_4 (Figure 8e,f) are reported in the potential range from −2.2 V versus Fc/Fc^+ to −1.9 V versus Fc/Fc^+, and the data are summarized in Table S7 (Supporting Information). The maximum Faradaic efficiency for all three metal oxalate salts was observed at the more positive potential −1.9 V versus Fc/Fc^+. However, the largest PCD for metal oxalate production occurs at the most negative potential investigated, −2.2 V versus Fc/Fc^+. Because all oxalate salts showed the highest FE at −1.9 V versus Fc/Fc^+, we compared the FE and PCD of CoC_2O_4, FeC_2O_4, and MnC_2O_4 on the same plot with ZnC_2O_4 at this potential in Figure S11a,b (Supporting Information). We see that, at this potential, TP-PTFE produces all four metal oxalate salts with roughly similar Faradaic efficiency. However, the partial current density going toward the production of FeC_2O_4 and ZnC_2O_4 are ≈1.7x that of CoC_2O_4 and MnC_2O_4. This suggests that the rate of degradation for Co and Mn is higher than that Zn and Fe and will be investigated in subsequent studies.

2.5. Characterization of MC_2O_4 Products

Following the CPEs, the solid individual metal oxalates were fully characterized following the methods outlined by Marx et al. (**Figure 9**).[65] Following ATR-FTIR, we measured the evolution of CO_2 from the dissolution of $C_2O_4^{2-}$ in aqueous H_2SO_4 as shown in Equation (6) (where M is Zn, Co, Fe, or Mn) and depicted in Figure 9a–d, following the procedure of Li et al.[66]

$$H_2SO_4\,(aq) + MC_2O_4\,(s) \rightarrow 2CO_2\,(g) + M^{2+}\,(aq) + SO_4^{2-}\,(aq) + 2H^+\,(aq) \quad (6)$$

A sample of the experimental solids was placed into a gas-tight sealed container, and aliquots of the headspace were measured using GC to establish a baseline chromatograph. Aqueous H_2SO_4 was then added to fully dissolve the solids in the sealed containers, and the headspace of the container after dissolution was measured. Peaks at 4 min were observed in the GC, consistent with CO_2 generation (Figure 9a–d). Analogous peaks were observed for the commercial oxalate standards investigated under identical conditions. As another method of characterization, ^{13}C NMR solutions of the experimentally generated solid, using isotopically labeled CO_2 to increase signal intensity, were prepared by dissolving the solids in ammonium hydroxide according to Equation (7)

$$MC_2O_4\,(s) + NH_4OH\,(aq) \rightarrow M^{2+}\,(aq) + C_2O_4^{2-}\,(aq) + NH_4^+\,(aq) + OH^-\,(aq) \quad (7)$$

The resulting ^{13}C NMR spectrum for the experimentally generated solids showed peaks at 174 ppm assigned to the C in $C_2O_4^-$ and analogous to the ^{13}C NMR spectrum of their respective commercial oxalate standards (Figure 9e–h). Representative experimental solids of 100 mg each are also shown in Figure 9i–l.

Additional characterization of the solids (shown in Figure 9i–l) included powder X-ray diffraction (PXRD) and X-ray photoelectron spectroscopy (XPS) measurements. The PXRD pattern of the experimentally generated solid product was similar to the measured diffraction patterns for commercial standards of each respective metal oxalate salt (Figures S12 and S13, Supporting Information). Additionally, XPS spectra of experimentally generated solid were consistent with those of the respective commercial standards as shown in Figures S14 and S15 (Supporting Information). Overall, these characterization studies all confirm that the solid electrolysis products of CPE by trace Pb is the C—C coupled products of MC_2O_4.

2.6. Postmortem Characterization of the Electrode Surface

We characterized the PTFE-coated electrode surfaces TP-PTFE and CP-PTFE before and after electrolysis via XPS and scanning electron microscopy (SEM) to look for any changes in surface speciation and morphology during the electrocatalytic process (**Figure 10**). XPS characterization of TP-PTFE revealed agglomeration of the polymer post electrolysis. This agglomeration post electrolysis is also seen in the SEM images in Figure 10g–i. Before electrolysis, XPS analysis showed the characteristic spectroscopic signature of the PTFE layer in the electrode at 292.6 eV in the C 1s core scans corresponding to the polymer backbone, —CF_2 (Figure 10a,d).[67–69] Post electrolysis, the C 1s core scan shows emerging features at 284.8 eV (C—C) and 291

© 2025 The Author(s). Advanced Energy Materials published by Wiley-VCH GmbH

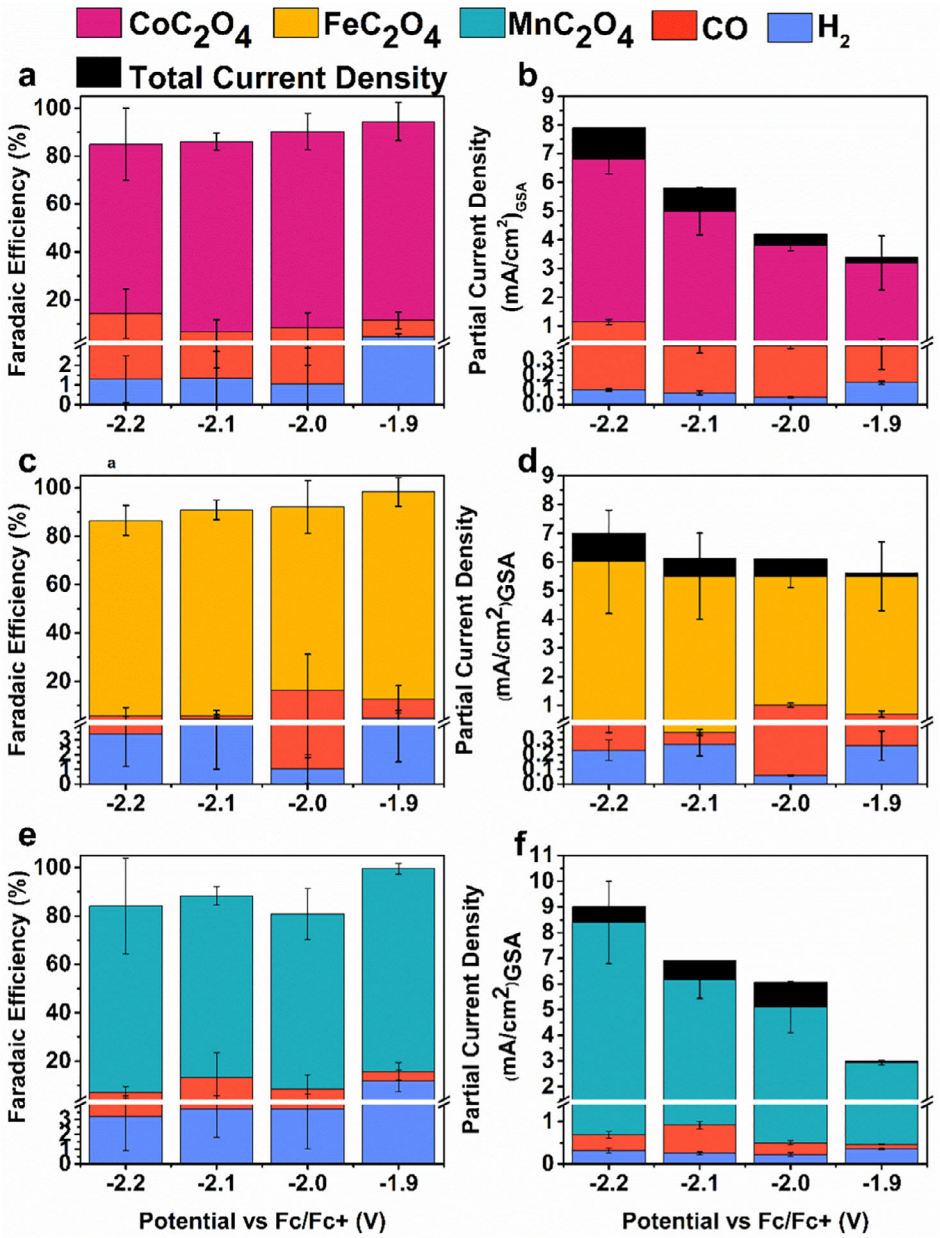

Figure 8. Product distributions and partial current densities from CPE measurements for the CO_2R by TP-PTFE with a,b) Co, c,d) Fe, and e,f) Mn foil counter electrodes in CO_2-saturated 0.1 M nBuClO$_4$ in MeCN. CPEs were conducted for 100 C at four different potentials: −1.9, −2.0, −2.1, and −2.2 V versus Fc/Fc$^+$. All data in this figure are also included in Table S7 (Supporting Information).

eV (—CF—),[69] showing exposure of the underlying layer consistent with agglomeration of the polymer exposing the underlying surface (Figure 10b,c,e,f). In addition, the emerging peak at 289 eV (O—C=O) post electrolysis is consistent with the presence of residual ZnC_2O_4 on the surface.[70,71] Note that the F 1s XPS core scans show a single peak at 689.6 eV corresponding to a —CF_2— functional group[67] that remains the same post electrolysis, indicating that the PTFE layer is stable on the surface of the electrode during the electrocatalytic process. Note that the loading of Pb on these surfaces is sufficiently small such that it is below the detection limit of XPS. In addition, XRD measurements of TP-PTFE and CP-PTFE surfaces' pre-electrolysis showed no peaks in the diffractograms, consistent with an amorphous polymer coating the electrode surface. However, post electrolysis, the XRD diffractograms showed peaks associated with the underlying electrode, consistent with polymer agglomeration exposing the underlying carbon support (Figure S16, Supporting Information). We see similar evidence of agglomeration in the postmortem characterization of CP-PTFE using XPS and SEM (Figure S17, Supporting Information) as well as the XPS of TP-PTFE with different SAs (Figure S18, Supporting Information).

We also investigated changes to the composition of the electrode after the electrolysis experiments. Energy dispersive spectroscopy (EDS) measurements of the surface suggest no change

© 2025 The Author(s). Advanced Energy Materials published by Wiley-VCH GmbH

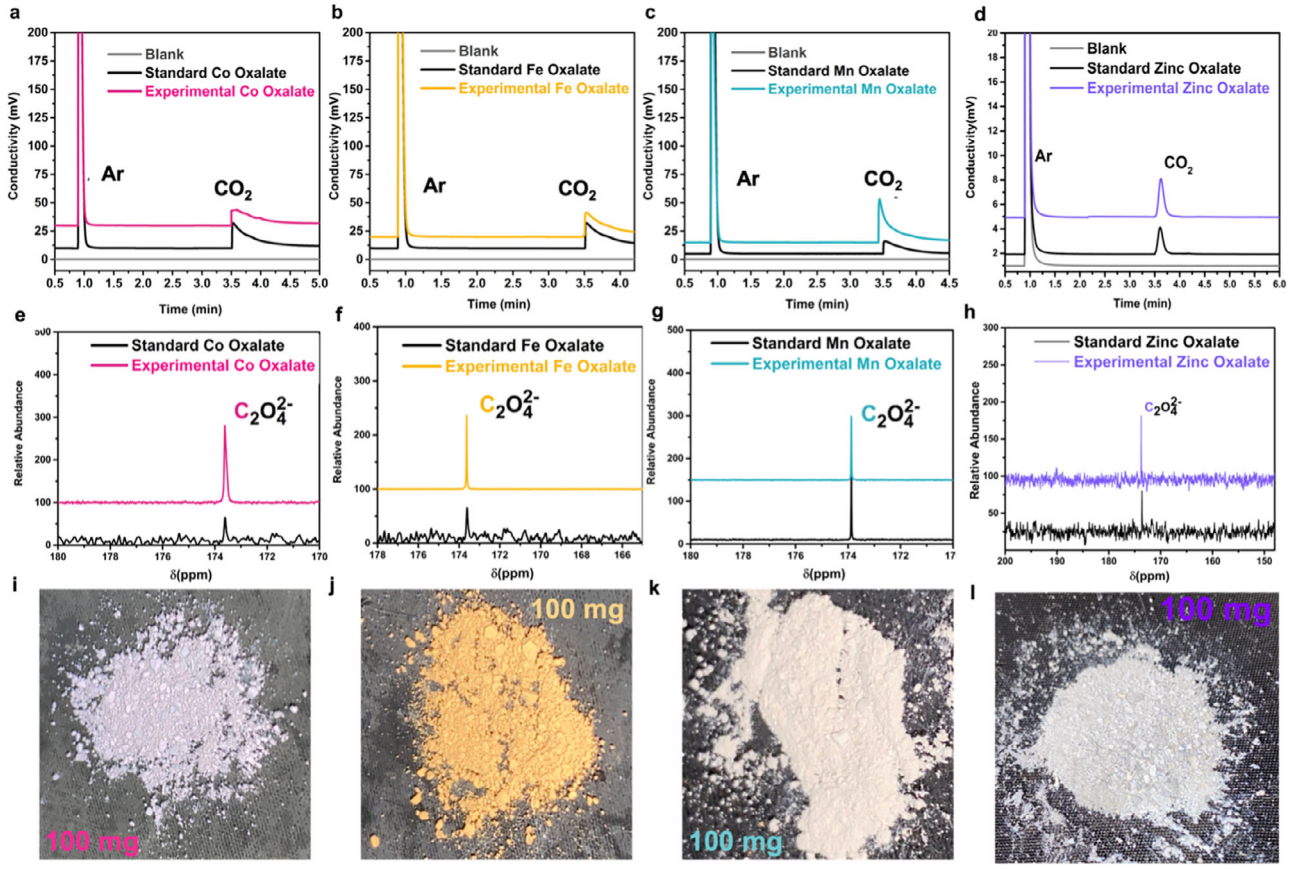

Figure 9. Characterization of the experimentally generated MC_2O_4 solids compared to a commercial MC_2O_4 standards by a–d) GC-TCD of the headspace after digestion of the solids in aqueous H_2SO_4. e–h) ^{13}C NMR of standards and experimental solids. i–l) A representative photograph of the MC_2O_4 solids produced during electrolysis.

in the C and F compositions of the TP-PTFE electrode post electrolysis (Figure S19, Supporting Information) the Pb loading was below the limit of detection for EDS. ICP-MS measurements of electrodes TP and TP-PTFE post electrolysis show analogous Pb loadings to as-prepared electrodes, suggesting minimal loss of Pb during the electrolysis (Table S8, Supporting Information).

Overall, these measurements suggest that the composition of the surface is largely unchanged during the electrolysis measurements. However, for the PTFE-coated electrodes, the PTFE layers agglomerates during the electrode, exposing more of the underlying electrode surface. This agglomeration and surface exposure may explain why the PTFE-coated electrodes show such similar overall activity to the bare carbon electrodes, albeit with higher selectivity for MC_2O_4—the agglomeration exposes more of the trace-Pb on the electrode surface, but the fluoropolymer layer still provides a sufficiently tailored microenvironment to facilitate selective reduction of CO_2 to $C_2O_4^{2-}$.

2.7. Control Experiments to Confirm CO_2R Activity

To confirm that all MC_2O_4 production in our electrolyses is due to CO_2 reduction at trace metal Pb sites, we conducted several control experiments in which the parameters for a typical electrolysis was conducted with only one parameter being changed. These control experiments were specifically chosen to ensure MC_2O_4 production was from CO_2R and not from a side reaction or any other anomalous process within the cell during the CPEs. The following experiments were conducted using electrochemical cells with all SAs (Zn, Co, Fe, and Mn). However, for clarity, Figures S20–S24 (Supporting Information) present representative data from experiments with Zn SAs, as the metal cations in these metal oxalate salts are interchangeable, as demonstrated by our characterization.

$^{13}CO_2$ isotopic labeling experiments were conducted to confirm that all MC_2O_4 comes from CO_2R and not other potential carbon sources. CPEs were conducted at a TP-PTFE electrode in MeCN with 0.1 M nBu$_4$ClO$_4$ under a $^{13}CO_2$ atmosphere. ATR-FTIR (Figure S20, Supporting Information) and matrix-assisted laser desorption/ionization mass spectrometry (MALDI-MS) (Figure S21, Supporting Information) were used to confirm that the solid product produced during the electrolysis was $M^{13}C_2O_4$. ATR-FTIR of our experimentally generated $M^{13}C_2O_4$ as a product of the CPE experiments under $^{13}CO_2$ showed a characteristic redshift for all carbon-related bending and stretching peaks compared to a commercial unlabeled MC_2O_4 standard (Figure S20, Supporting Information). The experimentally

© 2025 The Author(s). Advanced Energy Materials published by Wiley-VCH GmbH

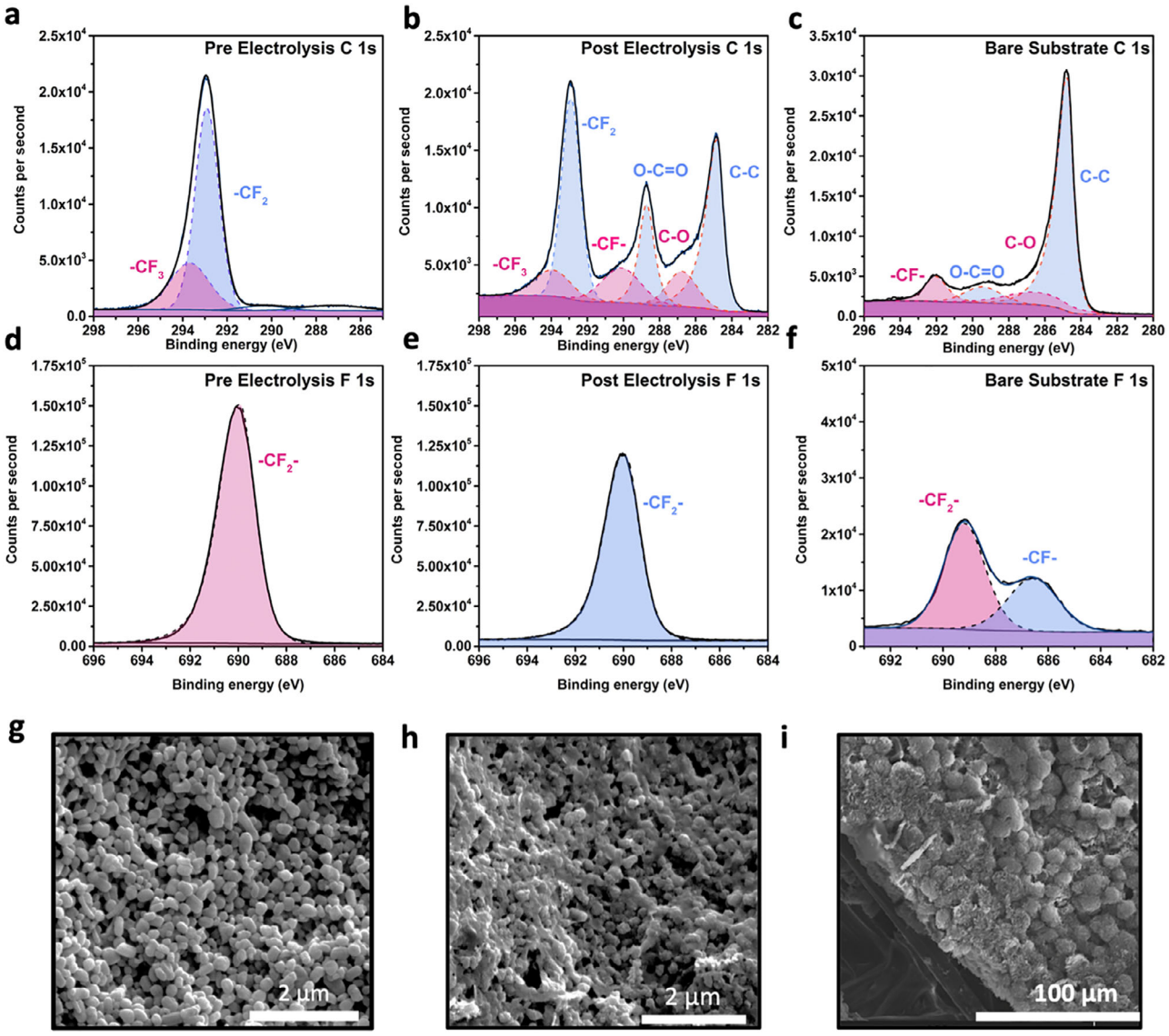

Figure 10. Postmortem characterization of the TP-PTFE electrode. a–c) Representative high-resolution XPS spectra in the C 1s region of a) as-prepared TP-PTFE, b) TP-PTFE post electrolysis, and c) the underlying TP electrode. d–f) Representative high-resolution XPS spectra in the F 1s region of d) as-prepared TP-PTFE, e) TP-PTFE post electrolysis, and f) the underlying TP electrode. g–i) Representative SEM images of g) as-prepared TP-PTFE, h) TP-PTFE post-electrolysis, and i) the underlying TP electrode.

generated $M^{13}C_2O_4$ was also characterized by MALDI-MS. Using a high-resolution mass spectrometry system, we were able to obtain accurate mass-to-charge ratios (m/z) showing $m/z = 91$ for experimentally generated $M^{13}C_2O_4$ compared to $m/z = 89$ for a commercial unlabeled MC_2O_4 sample. By using a high resolving power mass spectrometry system, we obtained highly accurate mass-to-charge ratios (m/z) of both the isotopically labeled and nonlabeled metal oxalate ion. These experiments support our assertation that MC_2O_4 produced during our CPE experiments is indeed from the reduction of dissolved CO_2 contaminant.

Out of an abundance of caution, we also conducted other control experiments. To confirm that MC_2O_4 is only produced during CPEs in the presence of CO_2, control CPEs were conducted using TP, TP-PTFE, and CP-PTFE electrodes under both an Ar atmosphere and air atmosphere. In all cases, no MC_2O_4 was formed when CO_2 was not present in the system. To confirm that the MC_2O_4 production was not due to solvent contaminant, we also conducted CPEs using TP-PTFE electrodes under CO_2 in 0.1 M nBu$_4$ClO$_4$ in propylene carbonate. In this new propylene carbonate solvent, we also detected MC_2O_4 production (Figure S22, Supporting Information) suggesting that the product is not due to a solvent-specific artifact or contaminant in MeCN. We also substituted nBu$_4$ClO$_4$ with tetrapropylammonium perchlorate (nPr$_4$ClO$_4$) in our electrolyses to ensure that MC_2O_4 is not due to some electrolyte-specific contaminant. CPEs conducted using TP-PTFE electrodes in 0.1

© 2025 The Author(s). Advanced Energy Materials published by Wiley-VCH GmbH

M nPr_4ClO_4 in MeCN under CO_2 atmosphere still produced MC_2O_4 as shown in Figure S23 (Supporting Information).

To confirm that the PTFE polymer not undergoing any non-Faradaic process resulting in MC_2O_4 production, we reproduced the CPE experiments on CP-PTFE electrodes coated with an alternative polymer source, poly(vinylidene fluoride) (PVF) as well as polyacrylic acid (PAA). The resulting CP–PVF electrodes also showed MC_2O_4 formation and CP–PAA showed MCO_3 formation (Figure S24, Supporting Information), indicating that the polymer enhancement of MC_2O_4 can be reproduced with other polymer sources. Finally, to confirm that MC_2O_4 production during the CPEs is not due to some leachate from the electrode or cell, we prepared our TP–PTFE electrode in our sealed CPE cell in 0.1 M nBu_4ClO_4 in MeCN under Ar atmosphere and held the cell at open circuit for 12 h. No products were detected after 12 h at open circuit, confirming that MC_2O_4 production is not produced from some cell or electrode leachate. These control experiments, combined with the $^{13}CO_2$ labeling experiments, confirm that MC_2O_4 is produced from the electrochemical reduction of CO_2 and not because of some side reaction or system contaminant.

3. Conclusions

In this work, we have shown that porous carbon supports containing trace (≤160 ng) loadings of metallic Pb are active electrocatalysts for CO_2 reduction to $C_2O_4^{2-}$ in nonaqueous solutions. In the presence of M^{2+} ions from a sacrificial anode, this electrogenerated oxalate precipitates as solid MC_2O_4. Notably, a commercial CP with ≈150 ng cm^{-2} of Pb contamination was only marginally active for CO_2 reduction to CO, but exhibited high activity and selectivity for $C_2O_4^{2-}$ formation when coated with a PTFE overlayer. In contrast, a TP support with higher Pb content (≈790 ng cm^{-2}) was active toward MC_2O_4 formation even without polymer modification, and PTFE coatings did further improve its performance.

These results, along with Pb loading studies on CP electrodes, suggest the existence of a threshold Pb loading required to facilitate C—C coupling during CO_2 reduction, and that this threshold is effectively lowered by modifying the local environment with a PTFE overlayer. Once this threshold is surpassed, increasing Pb loading does not significantly enhance the activity or selectivity for MC_2O_4 formation. For example, trace-Pb-loaded CP–PTFE and TP electrodes achieve similar selectivity and current density for ZnC_2O_4 as bulk Pb electrodes, implying that their turnover frequencies and mass activities are substantially higher.

The product selectivity for $C_2O_4^{2-}$ over CO_3^{2-} can be sensitive to several parameters, including the presence of cations or water molecules near the electrode surface that stabilize adsorbed $*CO_2^{\bullet-}$ and promote carbonate formation over C—C coupling. We postulate that the PTFE overlayer produces a favorable microenvironment for CO_2R to $C_2O_4^{2-}$ by both 1) helping to retain $*CO_2^{\bullet-}$ at or near the electrode surface to promote C—C coupling and 2) inhibiting the transport of electrolyte cations (e.g., nBu_4^+) and trace water that could otherwise stabilize $*CO_2^{\bullet-}$ and steer the reaction toward carbonate.

To evaluate the broader utility of this system, we extended the platform to the electrosynthesis of other metal oxalates—namely CoC_2O_4, FeC_2O_4, and MnC_2O_4—by varying the sacrificial anode. These oxalates are of particular interest for their potential application in sustainable cementitious materials. Isotopic labeling experiments confirmed that these products originate from CO_2. Altogether, our findings demonstrate that trace amounts of Pb can achieve catalytic performance on par with bulk Pb electrodes for CO_2-to-oxalate conversion, and that this activity can be significantly enhanced through deliberate microenvironment design. This approach may provide a general strategy for selective C_2 product formation using trace metal species. At the same time, the results underscore the need for caution in interpreting electrocatalytic performance when using carbon-based supports (CBS), as trace-metal contaminants—undetectable by standard compositional analysis—can meaningfully contribute to observed reactivity.

4. Experimental Section

Chemicals and Materials: Acetonitrile (anhydrous 99.8%), tetrabutylammonium perchlorate (electrochemical analysis, ≥99.0%), Zn, Fe, Co, and Mn foil (99.999% trace metal basis), lithium chloride (ACS reagent, ≥99%), PTFE powder (free flowing, 1 µm particle size), HNO_3 (trace metal grade, 67–70%), isopropyl alcohol (anhydrous, 99.5%), Pb powder (100 mesh, 99.95% trace metals basis), poly(vinylidene fluoride) (average M_w ≈ 534 000 by GPC, powder), poly(acrylic acid) (average M_v ≈ 450 000), zinc carbonate basic (>58% Zn basis), and zinc oxalate hydrate were used as purchased from Sigma–Aldrich. The standard calibration solutions (1000 ppm ± 3% in 5 wt% HNO_3) of Pb used for ICP-MS were purchased from RICCA Chemical Company. Research-grade CO_2 (99.999%) was used as purchased from Matheson Gas, and Ag/AgCl reference electrodes were purchased through ALS Japan. Toray Carbon Paper (TGP-H-060) was purchased from Fuel Cell Earth (purchase sources for all electrodes can be found in Table S1, Supporting Information). Ethanol (anhydrous, 200 proof) was purchased from KOPTEC and used as was with 18.2 MΩ cm^{-1} water from a Thermo-Fisher Barnstead E-pure purification system.

Electrochemical Synthesis: The electrolysis cell used in these experiments was an airtight and undivided borosilicate glass compartment equipped with gas inlets and outlets, as well as a three-electrode system. All glassware was heated overnight to remove adsorbed water vapor and cleaned with high-purity nitrogen to remove dust particles prior to each use. The typical electrolyte was 0.1 M nBu_4ClO_4 dissolved in MeCN prepared in an isolation chamber under argon prior to being added to the prepared cell. In a typical cell the working electrode consisted of a carbon-based support with or without PTFE ink with a geometric surface area of ≈1 cm^2, the counter electrode was a sacrificial metal plate, and the reference electrode was Ag/AgCl with 0.04 M LiCl and 0.1 M nBu_4ClO_4 solution in MeCN. 100 C was passed for all experiments and the condition of the cell over time is shown in Figure S25 (Supporting Information). All metal oxalate products were extracted from the electrochemical cell and washed with ethanol followed by ultrapure deionized water (18 MΩ), and 0.1 M sodium hydroxide to remove residual electrolyte as well as trace $(MCO_3)_2{\bullet}(M(OH)_2)_3$ and were then dried at 100 °C for 24 h prior to gravimetric analysis.

Ink and Electrode Preparation: In a typical experiment an ink was prepared with 1000 µL of Isopropanol (IPA) and 23.5 mg of PTFE powder. The mixture was sonicated for 90 min prior to spray deposition where a Master Airbrush coating system with TC-20 compressor and a 0.3 mm tip was used to dispense 400 µL of ink on each electrode used. All electrodes with two conductive sides were coated with epoxy on one side to control catalytic surface area. A description of all electrodes used can be found in Table S1 (Supporting Information).

Pb Loading Electrodes: For the Pb loading experiments all carbon paper electrodes were first etched in HNO_3 and water at a 1:8 ratio and heated at 70 °C overnight. These were then dried in an oven and moved into a glovebox for electrode preparation. A Pb ink was made by using 100 mg of Pb in

© 2025 The Author(s). Advanced Energy Materials published by Wiley-VCH GmbH

10 mL of MeCN and under constant stirring the Pb desired Pb amount was dropcasted onto the prepared carbon electrodes. For these experiments, everything including the cell was done in an inert atmosphere.

Characterization: NMR: Generated zinc oxalate powder was dissolved in 30% NH_4OH, and aliquots of the solution were analyzed using a 400 MHz Bruker NMR spectrometer with a tetramethylsilane (TMS internal standard and $(CD_3)_2CO$.

Characterization: MALDI-MS: Measurements were performed on a Bruker timstof fleX dual source MALDI-MS system. Samples were mixed with saturated 1,5-diaminonaphthalene (DAN) MALDI matrix solution composed of 1:3 water:methanol (v:v) and was spotted onto an indium–tin oxide coated glass slide. The use of DAN enabled both positive and negative ion modes to be tested and did not result in an isobaric ion at the same *m/z* value as either the isotopically labeled or nonlabeled ion. The mass spectra were acquired from *m/z* 50 to 500 using a method optimized for small-molecular-weight ions. In brief, 150 laser shots at 80% laser energy were used for ionization of the zinc oxalate ion in negative ion mode. The instrument was calibrated using a quadratic calibration of Agilent tune mixture, ensuring sub ppm mass accuracy.

Characterization: ATR-FTIR: Measurements were performed on a Bruker Tensor FTIR 27 with an ATR attachment. Scans were taken from 3600 to 600 wavenumbers. The experimentally generated solid was ground into a powder with mortar and pestle prior to scans.

Characterization: PXRD: Diffractograms from each solid were obtained using a Bruker Eco-Advance diffractometer equipped with a Cu Kα source (1.5406 Å).

Characterization: XPS: Photoelectron spectroscopy was carried out in a Kratos Supra Axis Spectrometer (Shimadzu corporation) with a monochromatic Al Kα source (1486.6 eV). Data were processed with the ESCApe software.

Characterization: SEM: Microscopic images of electrodes and powders were obtained with an FEI Nano Nova 430 scanning electron microscope. Due to the epoxy backing on the electrodes, they were sputtered with gold using a Quorum Tech Q150RES sputter coater before imaging. Typically, 5 nm of Au was sputtered onto electrodes.

Characterization: EDS: Spectra were obtained using an FEI Scios scanning electron microscope equipped with an energy dispersive X-ray spectroscope (Oxford Instruments). Both standard and experimentally generated zinc oxalate were placed on copper tape.

Characterization–Gas Chromatography-Thermal Conductivity Detector (GC-TCD): Measurements were taken with a Thermo-Fisher GC equipped with a Carboxen 1010 porous layer open tubular (PLOT) fused silica column (30 m × 0.53 mm × 10 µm), with helium as a reference and carrier gas. Acid digestion coupled with GC was completed by first using a 20 mL scintillation vial with a septa seal and ≈20 mg of standard zinc oxalate. The vial was then purged under argon for 20 min and then 5 mL of 0.5 M H_2SO_4 was added. This was stirred at 80 °C for 10 min and an aliquot of the headspace was taken for GC analysis. This procedure was repeated with the experimental zinc oxalate.

Characterization: ICP-MS: The metal contents in the electrodes were measured using ICP-MS (Perkin Elma Nexion 2000). To prepare the analyte for ICP-MS, 15 mL of 5 wt% trace metal grade HNO_3 solution was added to the mass of electrode substrate, the resulting mixture was stirred under 500 rpm for at least 48 h. The solution was then filtered using a cellulose syringe (0.45 µm, Titan 3 regenerated cellulose, Fisher Scientific) to remove any undissolved components. 1 mL of the filtered solution was diluted with 9 mL 1 M HNO_3 solution (1:9 v/v) to make the final analyte. The samples were then analyzed in ICP-MS using the Pb, Cr, Ni, and Hg calibration standards in 1 M HNO_3 at 0, 1, 5, and 20 ppb.

Characterization: Karl Fischer Titration: The water content in representative electrolyte solutions was measured via Karl Fischer titration. Briefly, methanol was used as the KF solvent to dissolve the samples. The titration was performed using a Coulometric Karl Fischer apparatus, calibrated prior to each use with a standard solution of known water content to ensure accuracy. Electrolyte samples were prepared in an inert atmosphere to minimize atmospheric water contamination.

WCA and ECA experiments were conducted using a CAM 100 (KSV Instruments) contact angle goniometer. The water used in this study was 18 MΩ water purified by a Millipore Milli-Q ultrapure water purification system. The nonaqueous electrolyte used for the contact angle measurements in this study was 0.1 M nBu$_4$ClO$_4$ in MeCN. Note that no effort was made to dry the MeCN in the electrolyte solutions used for the ECA measurements, and so it was expected for them to contain water concentrations between 0.4 and 0.14 M H_2O based on previously reported Karl Fisher titrations of commercial MeCN and similar electrolyte solutions.[72–74] Each dry electrode sample was placed horizontally on a platform, and a droplet of water or electrolyte was placed onto the area of interest. The droplet profile was recorded by the camera (1 frame s^{-1} for 10 s total), and the contact angle between the substrate and the water or electrolyte droplet was analyzed by the software automatically. Each measurement was replicated three times on each electrode.

Computational Slab model: The Pb-doped graphite with three layers with a cell dimension of about 12 Å × 11 Å was modeled. Several Pb-doped graphite surfaces, each with lead atoms substituted into different vacancy sites, were examined. The most stable configuration with isolated, non-stacked Pb atoms was chosen for all subsequent calculations.

Computational DFT Methods: DFT calculations were performed with the VASP program (version 5.4.4), using the revised Perdew-Burke-Ernzerhof (PBE) functional,[75] D3 dispersion correction,[76] and projector augmented wave (PAW) pseudopotentials.[77] The cutoff energy for the plane-wave basis set was set to 400 eV, and Gaussian smearing with a width of 0.1 eV was used. The convergence criteria were set to 10^{-6} eV and 0.02 eV Å^{-1} for electronic minimization and geometry optimization, respectively. All calculations are spin-unrestricted. Only the gamma k-point sampling in the reciprocal space of the Brillouin zone was used due to the large supercell used.

Computational GCDFT: To account for electrochemical potential in the calculations, the catalytic interface was treated as a grand canonical ensemble of electrons. To sample the free energy surface, different amounts of electrons were used to shift the work function, which was shifted additionally based on the initial charge of the adsorbate. The surface charging technique[78] with the ideal capacitor approximation was used to calculate the potential-dependent, grand canonical electronic free energy of the surface, ΔG, which is given by

$$\Delta G\left(U^{\mathrm{VAC}}\right) = \Delta E^{\mathrm{elec}}\left(U^{\mathrm{VAC}}\right) - q\left(U^{\mathrm{VAC}}\right) \mathrm{F} U^{\mathrm{VAC}}$$
$$\approx \Delta E^{\mathrm{elec}}\left(U_0^{\mathrm{VAC}}\right) - \frac{1}{2} C\left(U^{\mathrm{VAC}} - U_0^{\mathrm{VAC}}\right)^2 \quad (8)$$

where $\Delta E^{\mathrm{elec}}(U^{\mathrm{VAC}})$ is the electronic energy at U^{VAC}, the vacuum scale potential of the electrode, q is the number of supplied electrons to the system, F is the Faraday constant, $U_0{}^{\mathrm{VAC}}$ is the potential of zero charge, and C is the effective capacitance. The polarizable electrolyte region was represented by VASPsol[79] using a linearized Poisson–Boltzmann implicit solvation model. The dielectric constant of acetonitrile was used and set to 37.5. The Debye screening length was evaluated by

$$\lambda \approx \frac{3}{\sqrt{I}} \forall \quad (9)$$

where I is the ionic strength in molar concentration.[78] To model 0.1 M nBu$_4$ClO$_4$ used in the experiment, I was set to 0.1, and the thickness of the implicit solvent slab was increased to 90 Å.

Supporting Information

Supporting Information is available from the Wiley Online Library or from the author.

Acknowledgements

This work primarily was supported as part of the Center for Closing the Carbon Cycle, an Energy Frontier Research Center funded by the U.S. Department of Energy (DOE), Office of Science, Basic Energy Sciences (BES),

© 2025 The Author(s). Advanced Energy Materials published by Wiley-VCH GmbH

under Award Number DE-SC0023427. J.M.V. acknowledges initial support from a National Science Foundation CAREER Award (Award No. DMR-2044403, preliminary carbonate formation studies on uncoated carbon paper and toray paper), and from start-up funding from the University of California, Davis. J.M.V. also acknowledges additional support from a Camille Dreyfus Teacher Scholar Award and Alfred P. Sloan Foundation Award. XPS analysis at UC Davis was supported by the National Science Foundation under DMR-1828238.

Conflict of Interest

The authors declare no conflict of interest.

Author Contributions

R.S.B. contributed to conceptualization (equal), data curation (supporting), formal analysis (lead), investigation (lead), methodology (lead), validation (lead), visualization (equal), writing—original draft (lead), and writing—review and editing (equal). B.W.B. contributed to data curation (supporting), formal analysis (supporting), investigation (supporting), and writing—review and editing (supporting). S.C. contributed to data curation (supporting), formal analysis (supporting), investigation (supporting), visualization (supporting), and writing—reviewing and editing (supporting). J.T.P. contributed to conceptualization (supporting), methodology (supporting), and writing—review and editing (supporting). L.Y. contributed to formal analysis (supporting) and investigation (supporting). F.A. contributed to formal analysis (supporting) and investigation (supporting). C.A.N. contributed to investigation (supporting). Y.X. contributed to investigation (supporting). R.G.-C. contributed to investigation (supporting). A.K. contributed to investigation (supporting). E.K.N. contributed to data curation (supporting), investigation (supporting), and supervision (supporting). A.N.A. contributed to data curation (supporting), funding acquisition (equal), investigation (supporting), resources (supporting), supervision (supporting), and writing—reviewing and editing (supporting). C.C.L.M. contributed to conceptualization (supporting), data curation (supporting), funding acquisition (equal), project administration (supporting), resources (supporting), supervision (supporting), and writing—reviewing and editing (equal). J.M.V. contributed to conceptualization (equal), data curation (lead), funding acquisition (equal), project administration (lead), resources (lead), supervision (lead), visualization (equal), writing—original draft (supporting), and writing—reviewing and editing (equal).

Data Availability Statement

The data that support the findings of this study are available in the supplementary material of this article.

Keywords

alternative cementitious materials, carbon capture and utilization, carbon dioxide reduction, catalyst microenvironment, trace metal

Received: March 6, 2025
Revised: April 23, 2025
Published online: May 19, 2025

[1] The Role of Carbon Capture, Utilization, and Storage in Forming a Low Carbon Economy https://www.energy.gov/articles/role-carbon-capture-utilization-and-storage-forming-low-carbon-economy (accessed: June 2023).

[2] J. F. D. Tapia, J.-Y. Lee, R. E. H. Ooi, D. C. Y. Foo, R. R. Tan, *Sustainable Product. Consumption* **2018**, *13*, 1.
[3] J. C. Abanades, M. Akai, S. Benson, K. Caldeira, H. d. Coninck, P. Cook, O. Davidson, R. Doctor, J. Dooley, P. Freund, J. Gale, W. Heidug, H. Herzog, D. Keith, M. Mazzotti, B. Metz, L. Meyer, B. Osman-Elasha, A. Palmer, R. Pipatti, E. Rubin, K. Smekens, M. Soltanieh, K. Thambimuthu, *IPCC Special Report on Carbon Dioxide Capture and Storage*, Cambridge University Press, Cambridge, NY **2021**.
[4] What is CCUS and why is it necessary?, https://www.ief.org/news/what-is-ccus-and-why-is-it-necessary (accessed: June 2023).
[5] N. S. Lewis, *Science* **2016**, *351*, aad1920.
[6] N. S. Lewis, D. G. Nocera, *Proc. Natl. Acad. Sci. USA* **2006**, *103*, 15729.
[7] S. J. Davis, N. S. Lewis, M. Shaner, S. Aggarwal, D. Arent, I. L. Azevedo, S. M. Benson, T. Bradley, J. Brouwer, Y. M. Chiang, C. T. M. Clack, A. Cohen, S. Doig, J. Edmonds, P. Fennell, C. B. Field, B. Hannegan, B.-M. Hodge, M. I. Hoffert, E. Ingersoll, P. Jaramillo, K. S. Lackner, K. J. Mach, M. Mastrandrea, J. Ogden, P. F. Peterson, D. L. Sanchez, D. Sperling, J. Stagner, J. E. Trancik, et al., *Science* **2018**, *360*, eaas9793.
[8] N. S. Lewis, *Science* **2007**, *315*, 798.
[9] K. P. Kuhl, E. R. Cave, D. N. Abram, T. F. Jaramillo, *Energy Environ. Sci.* **2012**, *5*, 7050.
[10] Y. Hori, In *Handbook of Fuel Cells*, (eds W. Vielstich, A. Lamm, H. A. Gasteiger, H. Yokokawa), John Wiley & Sons, Ltd, **2010**.
[11] M. Jouny, W. Luc, F. Jiao, *Nat. Catal.* **2018**, *1*, 748.
[12] Y. Hori, I. Takahashi, O. Koga, N. Hoshi, *J. Phys. Chem. B* **2002**, *106*, 15.
[13] B. Eneau-Innocent, D. Pasquier, F. Ropital, J.-M. Léger, K. Kokoh, *Appl. Catal., B* **2010**, *98*, 65.
[14] S. Ikeda, T. Takagi, K. Ito, *Bull. Chem. Soc. Jpn.* **1987**, *60*, 2517.
[15] A. Gennaro, A. A. Isse, M.-G. Severin, E. Vianello, I. Bhugun, J.-M. Savéant, *J. Chem. Soc., Faraday Trans.* **1996**, *92*, 3963.
[16] M. König, J. Vaes, E. Klemm, D. Pant, *iScience* **2019**, *19*, 135.
[17] M. König, J. Vaes, D. Pant, E. Klemm, *J. Phys. Chem. C* **2023**, *127*, 18159.
[18] S. T. Erdogan, *AGU Fall Meeting Abstracts* **2017**, *2017*, S51C.
[19] S. T. Erdogan, *AGU Fall Meeting Abstracts* **2019**, *2019*, GC31E.
[20] Z. Luo, Y. Ma, H. He, W. Mu, X. Zhou, W. Liao, H. Ma, *J. Am. Ceram. Soc.* **2021**, *104*, 1120.
[21] E. Schuler, M. Demetriou, N. R. Shiju, G. J. M. Gruter, *ChemSusChem* **2021**, *14*, 3636.
[22] E. Ruiz-López, J. Gandara-Loe, F. Baena-Moreno, T. R. Reina, J. A. Odriozola, *Renewable Sustainable Energy Rev.* **2022**, *161*, 112329.
[23] V. Boor, J. E. Frijns, E. Perez-Gallent, E. Giling, A. T. Laitinen, E. L. Goetheer, L. J. Van Den Broeke, R. Kortlever, W. De Jong, O. A. Moultos, *Ind. Eng. Chem. Res.* **2022**, *61*, 14837.
[24] E. A. dos Reis, G. T. da Silva, E. I. Santiago, C. Ribeiro, *Energy Technol.* **2023**, *11*, 2201367.
[25] M. Jitaru, D. Lowy, M. Toma, B. Toma, L. Oniciu, *J. Appl. Electrochem.* **1997**, *27*, 875.
[26] W. Lv, R. Zhang, P. Gao, C. Gong, L. Lei, *J. Solid State Electrochem.* **2013**, *17*, 2789.
[27] C. Amatore, J. M. Saveant, *J. Am. Chem. Soc.* **1981**, *103*, 5021.
[28] P. C. Vesborg, T. F. Jaramillo, *RSC Adv.* **2012**, *2*, 7933.
[29] A. Kumar, A. Kumar, C.-P. MMS, A. K. Chaturvedi, A. A. Shabnam, G. Subrahmanyam, R. Mondal, D. K. Gupta, S. K. Malyan, S. S. Kumar, *Int. J. Environ. Res. Public Health* **2020**, *17*, 2179.
[30] M. F. C. Leal, R. I. Catarino, A. M. Pimenta, M. R. S. Souto, *Trace Elem. Electrolytes* **2023**, *40*, 1.
[31] X. Liu, P. Schlexer, J. Xiao, Y. Ji, L. Wang, R. B. Sandberg, M. Tang, K. S. Brown, H. Peng, S. Ringe, *Nat. Commun.* **2019**, *10*, 32.
[32] J. J. Lv, R. Yin, L. Zhou, J. Li, R. Kikas, T. Xu, Z. J. Wang, H. Jin, X. Wang, S. Wang, *Angew. Chem.* **2022**, *134*, 202207252.
[33] M. Ma, B. Seger, *Angew. Chem., Int. Ed.* **2024**, *63*, 2202401185.

© 2025 The Author(s). Advanced Energy Materials published by Wiley-VCH GmbH

[34] C.-T. Dinh, T. Burdyny, M. G. Kibria, A. Seifitokaldani, C. M. Gabardo, F. P. García de Arquer, A. Kiani, J. P. Edwards, P. De Luna, O. S. Bushuyev, *Science* **2018**, *360*, 783.
[35] Y. Hori, A. Murata, R. Takahashi, *J. Chem. Soc., Faraday Trans. 1* **1989**, *85*, 2309.
[36] Y. Hori, R. Takahashi, Y. Yoshinami, A. Murata, *J. Phys. Chem. B* **1997**, *101*, 7075.
[37] R. Kas, R. Kortlever, H. Yılmaz, M. T. Koper, G. Mul, *ChemElectroChem* **2015**, *2*, 354.
[38] Y. Liu, K. Y. Leung, S. E. Michaud, T. L. Soucy, C. C. McCrory, *Comments Inorg. Chem.* **2019**, *39*, 242.
[39] Y. Lum, Y. Kwon, P. Lobaccaro, L. Chen, E. L. Clark, A. T. Bell, J. W. Ager, *ACS Catal.* **2016**, *6*, 202.
[40] K. J. P. Schouten, E. P. Gallent, M. T. Koper, *J. Electroanal. Chem.* **2014**, *716*, 53.
[41] A. S. Varela, M. Kroschel, T. Reier, P. Strasser, *Catal. Today* **2016**, *260*, 8.
[42] L. Wang, S. A. Nitopi, E. Bertheussen, M. Orazov, C. G. Morales-Guio, X. Liu, D. C. Higgins, K. Chan, J. K. Nørskov, C. Hahn, *ACS Catal.* **2018**, *8*, 7445.
[43] D. V. Esposito, *ACS Catal.* **2018**, *8*, 457.
[44] F. Li, S.-F. Zhao, L. Chen, A. Khan, D. R. MacFarlane, J. Zhang, *Energy Environ. Sci.* **2016**, *9*, 216.
[45] S. Ponnurangam, C. M. Yun, I. V. Chernyshova, *ChemElectroChem* **2016**, *3*, 74.
[46] T. L. Soucy, W. S. Dean, J. Zhou, K. E. Rivera Cruz, C. C. McCrory, *Acc. Chem. Res.* **2022**, *55*, 252.
[47] Y. Zhao, X. Zu, R. Chen, X. Li, Y. Jiang, Z. Wang, S. Wang, Y. Wu, Y. Sun, Y. Xie, *J. Am. Chem. Soc.* **2022**, *144*, 10446.
[48] C. Kim, J. C. Bui, X. Luo, J. K. Cooper, A. Kusoglu, A. Z. Weber, A. T. Bell, *Nat. Energy* **2021**, *6*, 1026.
[49] N. E. Leadbeater, M. Marco, *Angew. Chem., Int. Ed.* **2003**, *42*, 1407.
[50] K. Y. Leung, C. C. McCrory, *ACS Appl. Energy Mater.* **2019**, *2*, 8283.
[51] I. Thome, A. Nijs, C. Bolm, *Chem. Soc. Rev.* **2012**, *41*, 979.
[52] L. Wang, A. Ambrosi, M. Pumera, *Angew. Chem.* **2013**, *125*, 14063.
[53] W. Kicinski, S. Dyjak, *Carbon* **2020**, *168*, 748.
[54] O. Akpoveta, S. Osakwe, *IOSR J. Appl. Chem.* **2014**, *7*, 1.
[55] R. R. Gagne, C. A. Koval, G. C. Lisensky, *Inorg. Chem.* **1980**, *19*, 2854.
[56] G. Gritzner, J. Kůta, *Electrochim. Acta* **1984**, *29*, 869.
[57] X. Han, M. Wang, M. L. Le, N. M. Bedford, T. J. Woehl, V. S. Thoi, *Electrochim. Acta* **2019**, *297*, 545.
[58] Y. Yoon, A. S. Hall, Y. Surendranath, *Angew. Chem., Int. Ed.* **2016**, *55*, 15282.
[59] T. Mairegger, H. Li, C. Grießer, D. Winkler, J. Filser, N. G. Hörmann, K. Reuter, J. Kunze-Liebhäuser, *ACS Catal.* **2023**, *13*, 5780.
[60] T. L. Soucy, Y. Liu, J. B. Eisenberg, C. C. McCrory, *ACS Appl. Energy Mater.* **2021**, *5*, 159.
[61] A. Bagger, O. Christensen, V. Ivaništšev, J. Rossmeisl, *ACS Catal.* **2022**, *12*, 2561.
[62] C. Deacon-Price, A. Mijatović, H. C. Hoefsloot, G. Rothenberg, A. C. Garcia, *ChemPhysChem* **2024**, *26*, 202400794.
[63] M. M. Cencer, C. Li, G. Agarwal, R. J. Gomes Neto, C. V. Amanchukwu, R. S. Assary, *ACS Omega* **2022**, *7*, 18131.
[64] J. J. Guerard, J. S. Arey, *J. Chem. Theory Comput.* **2013**, *9*, 5046.
[65] M. Marx, H. Frauendorf, A. Spannenberg, H. Neumann, M. Beller, *JACS Au* **2022**, *2*, 731.
[66] H. Li, Y. Liu, Q. Zhang, H. Zhan, *Anal. Methods* **2014**, *6*, 3720.
[67] C. Girardeaux, J.-J. Pireaux, *Surf. Sci. Spectra* **1996**, *4*, 138.
[68] J. M. Park, L. Matienzo, D. Spencer, *J. Adhes. Sci. Technol.* **1991**, *5*, 153.
[69] N. Vandencasteele, D. Merche, F. Reniers, *Surf. Interface Anal.* **2006**, *38*, 526.
[70] J. Ferreira, Jr, M. Oliveira, G. Trindade, L. Santos, C. Tomachuk, M. Baker, *Corros. Sci.* **2018**, *137*, 13.
[71] A. M. Salvi, F. Langerame, A. E. Pace, M. E. E. Carbone, R. Ciriello, *Surf. Sci. Spectra* **2015**, *22*, 21.
[72] Y. Hui, R. D. Webster, *Anal. Chem.* **2011**, *83*, 976.
[73] C. C. McCrory, N. K. Szymczak, J. C. Peters, *Electrocatalysis* **2016**, *7*, 87.
[74] D. B. G. Williams, M. Lawton, *J. Org. Chem.* **2010**, *75*, 8351.
[75] B. Hammer, L. B. Hansen, J. K. Nørskov, *Phys. Rev. B* **1999**, *59*, 7413.
[76] S. Grimme, J. Antony, S. Ehrlich, H. Krieg, *J. Chem. Phys.* **2010**, *132*, 154104.
[77] G. Kresse, D. Joubert, *Phys. Rev. B* **1999**, *59*, 1758.
[78] S. N. Steinmann, P. Sautet, *J. Phys. Chem. C* **2016**, *120*, 5619.
[79] K. Mathew, R. Sundararaman, K. Letchworth-Weaver, T. A. Arias, R. G. Hennig, *J. Chem. Phys.* **2014**, *140*, 084106.

© 2025 The Author(s). Advanced Energy Materials published by Wiley-VCH GmbH